nature communications

Article

https://doi.org/10.1038/s41467-025-63637-2

Asymmetric coordination enhances the synergy of Pt species dual active sites for efficient photocatalytic H_2 evolution

Received: 18 January 2025

Accepted: 26 August 2025

Published online: 12 September 2025

Check for updates

Bo Li[1], Hongshun Zheng[1,2], Tong Zhou[1] ✉, Qingjie Lu[1], Mingpeng Chen[1], Huachuan Sun[1], Yuxiao Zhang[3], Yumin Zhang[1], Dequan Li[1,2], Baoye Zi[1], Mao Zhang[3], Jin Zhang[1], Jianhong Zhao[1], Tianwei He[1], Zhongqi Zhu[1], Genlin Zhang[1] & Qingju Liu[1,2] ✉

Integrating distinct functional reaction sites within a single photocatalyst offers a promising approach for enhancing the photocatalytic H_2 evolution by water splitting. However, the synergy between the dual active sites is hindered by suboptimal electronic states arising from the uniform coordination environments. Here we demonstrate a strategy for enhancing the synergy between Pt single atoms and nanoparticles by modulating the coordination environment. The optimal boron doped catalyst with B-Pt-O asymmetric coordination achieves a H_2 evolution rate of 627.6 mmol $g^{-1}h^{-1}$, with an apparent quantum efficiency of 98.4%. Experimental and theoretical analysis reveal that the asymmetric coordination structure redistributes the electron density of Pt cocatalysts, promoting charge carrier separation, optimizing the dissociation and adsorption-desorption of the intermediate H_2O^* and H^* on the dual sites. The findings highlight the importance of asymmetric coordination facilitates the photogenerated carrier transfer and surface reactions for efficient photocatalytic H_2 evolution.

The efficient generation and utilization of hydrogen (H_2) remains a core objective in catalysis research, driven by the global pursuit of sustainable energy solutions[1–3]. Photocatalysis presents a promising pathway to convert solar energy into green H_2 via water splitting[4–6]. However, the current photocatalytic performance is constrained by poor light harvesting, high photogenerated carrier recombination, slow proton reduction kinetics, and the high energy barrier for activating the water reactants[7,8]. Particularly, charge-separation transfer represents a kinetically suppressive yet crucial step that determines the efficiency of subsequent surface redox reactions[9]. Overcoming these obstacles is vital to unlocking the potential of photocatalysts. Modifying the semiconductor surface with cocatalysts is an effective strategy for enhancing photocatalytic performance, which improves the separation and transfer of charge carriers, introduces additional active sites for the redox reactions and lowers the activation energy[10,11]. Moreover, the size of the cocatalyst significantly affects the activation of reactant molecules and the desorption of product molecules, both of which are crucial for maintaining photocatalytic efficiency[12].

In the photocatalytic H_2 evolution reaction (HER), single atoms (SAs) cocatalysts have demonstrated high intrinsic activity, attributed to their nearly 100% atomic utilization efficiency and defined electronic and structural properties. Nevertheless, SAs often struggle to activate water molecules[13–15], a challenging and potentially rate-determining step in HER[16,17]. Recent studies have increasingly focused on the role of nanoclusters/nanoparticles (NCs/NPs) in catalysis[18–20], which combine the high atomic utilization efficiency with metallic properties for facilitating the activation of H_2O molecules. A promising approach is integrating distinct functional reaction sites

[1]Yunnan Key Laboratory for Micro/Nano Materials & Technology, National Center for International Research on Photoelectric and Energy Materials, School of Materials and Energy, Yunnan University, Kunming 650091, China. [2]Southwest United Graduate School, Kunming 650091, PR China. [3]School of Engineering, Institute of International Rivers and Eco-security, Yunnan University, Kunming 650091, China. ✉e-mail: tongzhou@mail.ynu.edu.cn; qjliu@ynu.edu.cn

within a single photocatalyst to address the limitations of SAs cocatalysts, particularly for multi-step reactions such as photocatalytic water splitting. Some studies have highlighted the synergy between Pt SAs and Pt NC/NPs on oxide semiconductor supports in the photocatalytic H_2 evolution (PHE) by water splitting[14,21–23]. In this system, the Pt SAs serve as H* reduction sites, while the adjacent Pt NC/NPs are the activation sites of H_2O molecules. This spatially coupled heterogeneity creates dual active sites that complement the distinct functions, boosting the overall photocatalytic performance[24]. Besides, the electronic states of the NPs and SAs sites are crucial for the adsorption-desorption processes and the selectivity of reactants[25–27]. To further enhance the synergistic effect of the NP and SA sites in promoting the photocatalytic activity of SA&NP-based catalysts, it is essential to employ appropriate methods for modulating the electronic state of the dual sites.

The modulation of the local coordination environment of the active sites, encompassing the regulation of coordination atom type and coordination number, can optimize the electronic state and enhance the metal-support interactions (MSI)[28,29], thereby improving the activity. In particular, introducing heteroatoms into the first coordination shell of the metal single-atom active site forms an asymmetric coordination structure, typically represented by the Ha-M-Oa bonding configuration (Ha: Heteroatom; M: metal centre atom; Original coordination atom)[25,30]. This structural modification induces a redistribution of electron density due to the disparity in electronegativity between the heteroatoms and original coordination atoms, optimizing the desorption and conversion of reactants in electron deficient regions[31]. Moreover, the hybridization of the *d-p* orbital between the non-metallic heteroatoms and metallic active centre atoms can significantly alter the spin polarization of the active centre and further affect the catalytic activity[32,33]. Hence, the electronic states of dual active sites can be optimized to achieve enhanced photocatalytic efficiency by strategically incorporating heteroatoms asymmetric coordination.

Here, we developed an SAs&NPs-based photocatalyst featuring an asymmetric coordination structure. Titanium dioxide (TiO_2) was selected as the substrate for modification due to its stability and wide availability[33,34]. Meanwhile, Pt served as the cocatalyst for its intrinsic activity and electronic properties[35,36]. To construct the asymmetric coordination environment, boron (B) was introduced as a heteroatom, capitalizing on its well-documented role as an electron-modulating dopant with trivalent electronic characteristics($2s^2 2p^1$)[37], which can fine-tune the nucleophilicity of Pt for facilitating HER kinetics[38–40]. In the Pt-TiO_2-based catalysts, Pt atoms typically coordinate with O atoms[24,35]. The substitution of O with B creates a B-Pt-O coordination structure, which is anticipated to enhance photocatalytic performance by modulating electronic properties. Thus, a specialized metal-organic framework (MOF) precursor featuring Ti vacancies (MIL-125(Ti_V)) was utilized to anchor Pt atoms. The B species were introduced by a ligand substitution strategy, and the B-Pt-O coordination was eventually formed in the TiO_2 support by heat treatment. The resultant B doped and Pt-SAs&NPs loaded photocatalyst ($Pt_{SA/NP}$-$TiO_{2-x}B_x$) exhibits notable photocatalytic performance with a PHE rate of 627.6 mmol $g^{-1}h^{-1}$, and an apparent quantum efficiency (AQE) of 98.4% at 365 nm and a turnover frequency (TOF) of 33090 h^{-1}, outperforming the B-free counterpart. X-ray absorption fine structure (XAFS) analysis provides direct evidence for the B-Pt-O asymmetric coordination structure. Detailed investigations reveal that the asymmetric coordination structure leads to a redistribution of electron density between Pt SAs and NPs for optimizing the dissociation of H_2O* and adsorption-desorption of H* at the dual sites, and disrupts the balanced spin electrons to increasing spin polarization, for promoting the charge carrier separation and further enhancing the PHE reaction. The findings underscore the pivotal role of asymmetric coordination in optimizing dual-site catalysis and advancing PHE performance, providing a framework for developing cocatalyst semiconductor photocatalytic systems with high activity and stability.

Results and discussion

Morphology and structure characterizations of the photocatalysts

The $Pt_{SA/NP}$-$TiO_{2-x}B_x$ photocatalyst was synthesized via a multistep process, as illustrated in Fig. 1a. Initially, the MOF precursor with Ti_V was prepared using a previously reported hydrothermal method[10]. B species was introduced into the MOF structure through a ligand exchange strategy[41]. Subsequently, Pt was incorporated into the framework by an ion exchange process to fill the Ti_V. A final thermal treatment collapsed the MOF structure, thus B and Pt were uniformly dispersed within the TiO_2 lattice, yielding a B and Pt co-modified TiO_2 photocatalyst ($Pt_{SA/NP}$-$TiO_{2-x}B_x$). A control sample, $Pt_{SA/NP}$-TiO_2 (without B doping), was prepared following the same method, excluding the B ligand exchange step (refer to the Methods section for details).

X-ray diffraction (XRD) analysis confirms the successful synthesis of the MOF precursor, with the diffraction patterns of MIL-125 aligning with previous reports[10] (Supplementary Fig. 1a). The retention of characteristic peaks in the B-MIL-125(Pt) matches those of MIL-125 (Supplementary Fig. 1a), verifying the preserved MOF crystal structure. Fourier-transform infrared (FTIR) spectroscopy demonstrates the successful preparation of the B-modified MOF, as B-MIL-125 and B-MIL-125(Pt) exhibit three additional peaks (Fig. 1b), corresponding to B-O stretching vibrations (~1100 and ~1400 cm^{-1}) and B-C antisymmetric stretching vibrations (~1600 cm^{-1})[41,42]. Thermogravimetric analysis (TGA) reveals that the mass loss of B-MIL-125(Pt) ends at 450 °C (Supplementary Fig. 1b), representing the removal of organic components and the incorporation of thermally stable B and Pt species in the TiO_2. The XRD pattern (Fig. 1c) of the photocatalysts shows that pristine TiO_2 consists of anatase and rutile phases, while all the modified samples ($TiO_{2-x}B_x$, $Pt_{SA/NP}$-TiO_2, and $Pt_{SA/NP}$-$TiO_{2-x}B_x$) exhibit only anatase phases. This indicates that B and Pt atoms migrate into the TiO_2 lattice during the synthesis, modifying the local and short-range crystal structure and resulting in phase alterations, as evidenced by the weakened characteristic peaks. Samples with various contents of B and Pt were also analyzed (Supplementary Fig. 2a and b, XRD patterns), and no discernible peaks correspond to B_2O_3 and Pt species, confirming the high dispersion of B and Pt. Raman spectroscopy further confirms the substitutional B doping within the TiO_2 lattice (Fig. 1d), evidenced by the anatase characteristic peaks of $TiO_{2-x}B_x$ and $Pt_{SA/NP}$-$TiO_{2-x}B_x$ exhibiting a positive shift (~ 3 cm^{-1}) compared to TiO_2 and $Pt_{SA/NP}$-TiO_2, with no impurity peaks detected. The absence of the peak at ~ 820 cm^{-1} rules out the substitution of Ti by B, consistent with the previous conclusion that B preferentially substitutes O in the TiO_2 lattice[43], as its atomic radius closely matches that of O and requires minimal energy compared to substituting Ti or occupying interstitial sites[41,43]. Notably, the characteristic peaks of $Pt_{SA/NP}$-TiO_2 remain unchanged, consistent with the low content of Pt.

The morphology of the photocatalysts, as observed through scanning electron microscope (SEM) and transmission electron microscopy (TEM) (Fig. 1e and f and Supplementary Fig. 3a-d), shows that TiO_2 and $Pt_{SA/NP}$-TiO_2 retained the typical cake-like morphology of MIL-125, while $TiO_{2-x}B_x$ and $Pt_{SA/NP}$-$TiO_{2-x}B_x$ exhibit rough, square-like structures, which attributed to the atomic reconstruction during the high-temperature collapse of the MOF framework caused by B introduction. Brunauer-Emmett-Teller (BET) measurements reveal that $Pt_{SA/NP}$-$TiO_{2-x}B_x$ exhibits a larger specific surface area (SSA, 121.3 m^2g^{-1}, Supplementary Fig. 4c) and higher porosity (0.30 ml g^{-1}, Supplementary Fig. 4d) than that of $Pt_{SA/NP}$-TiO_2 (SSA, 88.7 m^2g^{-1}; porosity, 0.18 ml g^{-1}, Supplementary Fig. 4a and b), thanks to the rough morphology induced by B doping. Besides, the rough surface morphology improves the hydrophilicity of the catalysts, as evidenced by the lower water contact angles of $TiO_{2-x}B_x$ and $Pt_{SA/NP}$-$TiO_{2-x}B_x$ (Supplementary

https://doi.org/10.1038/s41467-025-63637-2

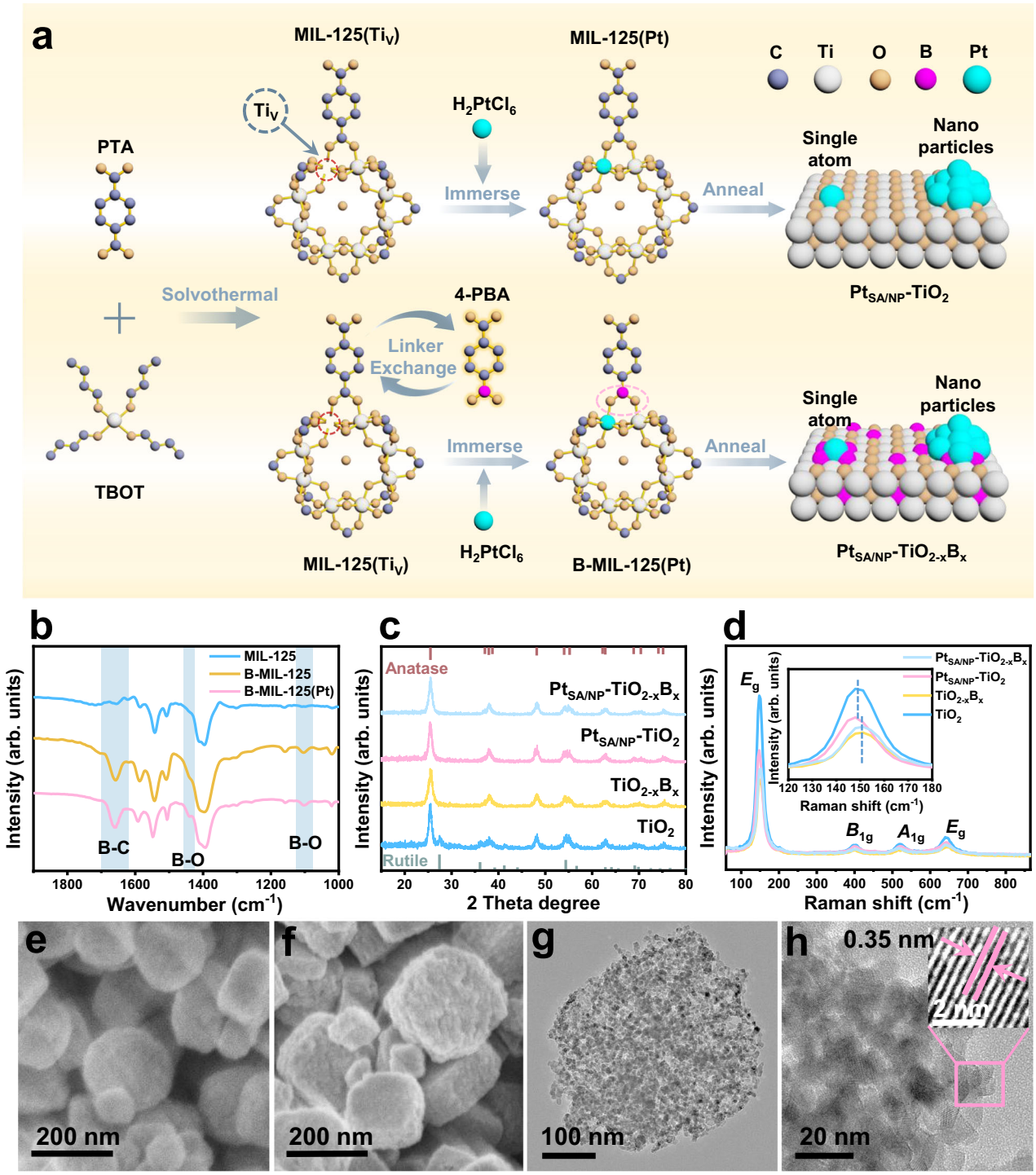

Fig. 1 | Synthesis and structure of the photocatalysts. a Synthetic process of $Pt_{SA/NP}$-TiO_2 and $Pt_{SA/NP}$-$TiO_{2-x}B_x$, PTA denotes 1,4-benzenedicarboxylic acid, TBOT denotes Titanium butoxide, 4-PBA denotes 4-Carboxyphenylboronic acid, H_2PtCl_6 denotes Chloroplatinic acid. **b** FT-IR spectra of MIL-125, B-MIL-125 and B-MIL-125(Pt). **c** XRD images of the photocatalysts. **d** Raman spectra of the photocatalysts. SEM images of **e** $Pt_{SA/NP}$-TiO_2 and **f** $Pt_{SA/NP}$-$TiO_{2-x}B_x$. **g** TEM images of $Pt_{SA/NP}$-$TiO_{2-x}B_x$. **h** High-resolution TEM images of $Pt_{SA/NP}$-$TiO_{2-x}B_x$. Source data are provided as a Source Data file.

Fig. 5a-d), which can facilitate the H_2O molecule adsorption for photocatalytic water splitting. TEM image (Fig. 1g) reveals that the TiO_2 consists of nanoscale crystalline grains and the photocatalysts exhibit regular cake-like morphology (Supplementary Fig. 6). $Pt_{SA/NP}$-$TiO_{2-x}B_x$ (Supplementary Fig. 8) shows a more porous and loosely packed structure compared to $Pt_{SA/NP}$-TiO_{2-x} (Supplementary Fig. 7), without observable aggregation. High-resolution TEM identifies the lattice fringes with a spacing of ~0.35 nm (Fig. 1h), corresponding to the anatase phase of TiO_2.

The aberration-corrected high-angle annular dark-field scanning transmission electron microscope (HAADF-STEM) was used to investigate the atomic structure of Pt species on the photocatalyst surface. As shown in Fig. 2a and Supplementary Fig. 9, Pt SAs and small Pt NPs are uniformly dispersed on both $Pt_{SA/NP}$-$TiO_{2-x}B_x$ and $Pt_{SA/NP}$-TiO_2

https://doi.org/10.1038/s41467-025-63637-2

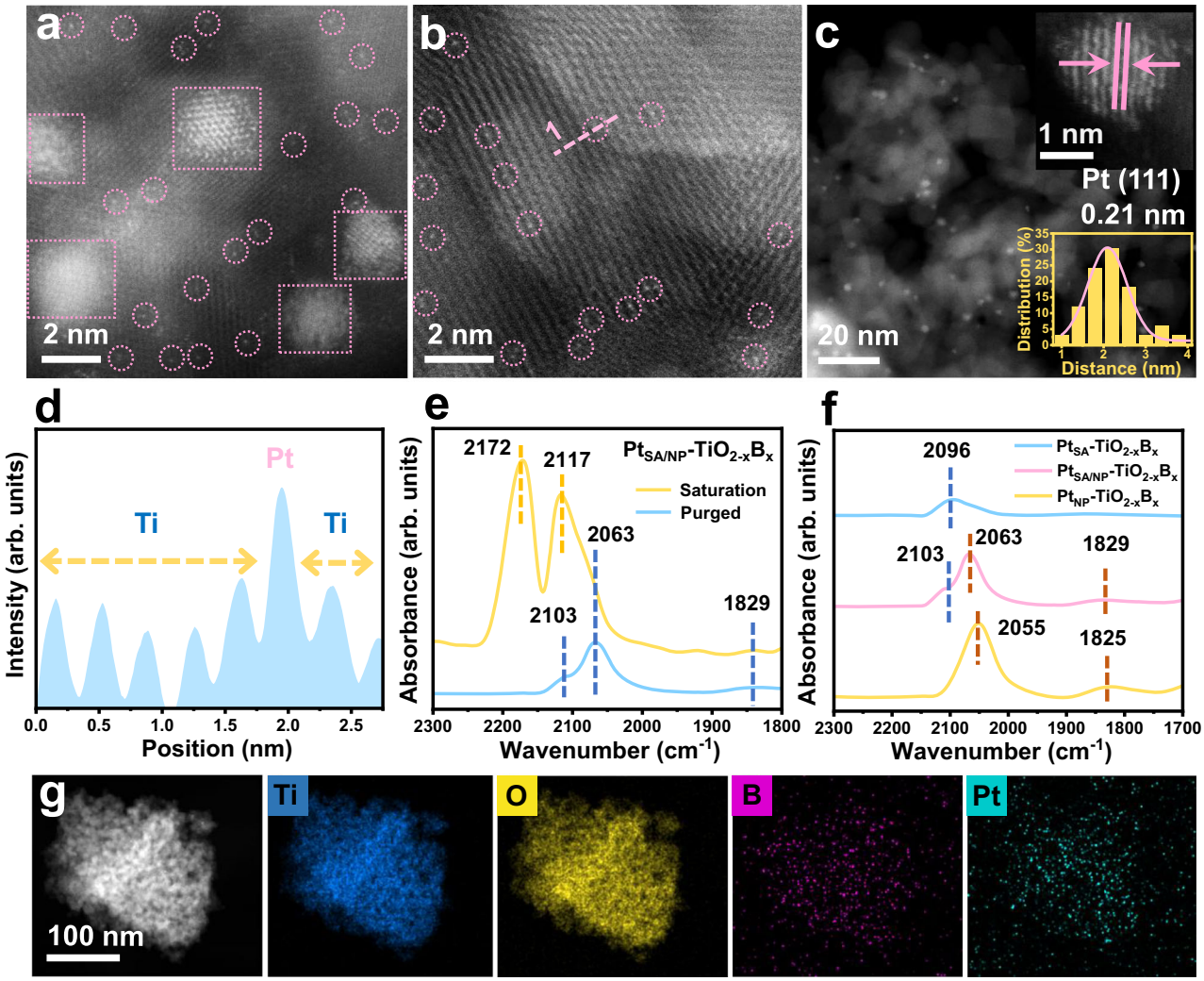

Fig. 2 | Microstructure of the cocatalysts. a, **b** HAADF-STEM images of $Pt_{SA/NP}$-$TiO_{2-x}B_x$. **c** HAADF-STEM, high-resolution image (inset), and the corresponding histogram of Pt_{NP} particle size distribution (inset) of the $Pt_{SA/NP}$-$TiO_{2-x}B_x$ photocatalysts, the NPs size ranges from 1 to 3.8 nm, with ~ 80% of the NPs falling between 1.5 and 2.5 nm, yielding an average size of 2.08 nm. **d** The corresponding atomic intensity profiles of Line 1 marked in **b**. **e** DRIFTS spectra of CO adsorption on $Pt_{SA/NP}$-$TiO_{2-x}B_x$. **f** CO-DRIFTS spectra of Pt_{SA}-$TiO_{2-x}B_x$, $Pt_{SA/NP}$-$TiO_{2-x}B_x$ and Pt_{NP}-$TiO_{2-x}B_x$, the peak at ~ 2096 cm^{-1} is assigned to linear CO adsorption on Pt SAs of Pt_{SA}-$TiO_{2-x}B_x$, and the peaks at ~ 2055 cm^{-1} and ~ 1825 cm^{-1} are attributed to linear and bridged CO adsorption on Pt NPs of Pt_{NP}-$TiO_{2-x}B_x$, respectively. **g** Ti, O, B and Pt element mappings of $Pt_{SA/NP}$-$TiO_{2-x}B_x$. Source data are provided as a Source Data file.

photocatalysts. The bright spots in the micrographs, attributed to the higher atomic number of Pt, correspond to Pt species. Specifically, Pt SAs and NPs are marked within dashed pink circles and boxes (Fig. 2a), respectively, confirming the coexistence of Pt SAs and NPs. Magnified views further illustrate the high dispersion of Pt SAs. The observed lattice fringes correspond to the arrangement of Ti atoms, and the individual bright spots along these fringes clearly represent Pt SAs (Fig. 2b), indicating that Pt atoms occupy the Ti sites. Atomic intensity profiles along the representative line corroborate this (Fig. 2d, Line 1 includes Ti and Pt atoms), the high-intensity signal of Pt contrasts with the lower intensity of Ti, confirming the presence of the Pt-O-Ti structural motif. The overall distribution and size statistics of Pt NPs are presented in Fig. 2c and Supplementary Fig. 10, showing a uniform dispersion with average grain sizes of 2.08 nm and 2.37 nm for $Pt_{SA/NP}$-$TiO_{2-x}B_x$ and $Pt_{SA/NP}$-TiO_2, respectively. The high-resolution image reveals a lattice spacing of 0.21 nm (Fig. 2c), consistent with the Pt (111) face, indicative of well-crystallized Pt NPs.

The CO adsorption behavior of Pt species was investigated using diffuse reflectance infrared Fourier transform spectroscopy (DRIFTS) to further confirm their dispersion properties and geometric configurations. As control samples, Pt_{SA}-$TiO_{2-x}B_x$ and Pt_{NP}-$TiO_{2-x}B_x$ containing only Pt SA and NP were synthesized, HAADF-STEM and XPS analyses verified the exclusive presence of SA and NP in the respective samples (refer to Supplementary Fig. 11 and 12). In the CO-DRIFTS spectrum of $Pt_{SA/NP}$-$TiO_{2-x}B_x$ (Fig. 2e), the peaks at ~ 2172 cm^{-1} and ~ 2117 cm^{-1} correspond to the vibrational modes of saturated gas-phase CO molecules[14]. After adequate purging, three distinct peaks associated with stable CO adsorption on Pt species were observed. The peak at ~ 2103 cm^{-1} is assigned to linear CO adsorption on Pt SAs[44], consistent with the characteristic signal observed in the Pt_{SA}-$TiO_{2-x}B_x$ (Fig. 2f). In contrast, the peaks at ~ 2063 cm^{-1} and ~ 1829 cm^{-1} are attributed to linear and bridged CO adsorption on Pt NPs[45,46], respectively, in agreement with the spectral features of the Pt_{NP}-$TiO_{2-x}B_x$ sample. The $Pt_{SA/NP}$-TiO_2 exhibits similar three peaks with $Pt_{SA/NP}$-$TiO_{2-x}B_x$ (Supplementary Fig. 13), further confirming the coexistence of SA and NP, which align with HAADF-STEM observations. Moreover, based on the deconvoluted peak areas in the CO-DRIFTS spectra (Supplementary Fig. 14) and the CO adsorption modes on Pt sites

https://doi.org/10.1038/s41467-025-63637-2

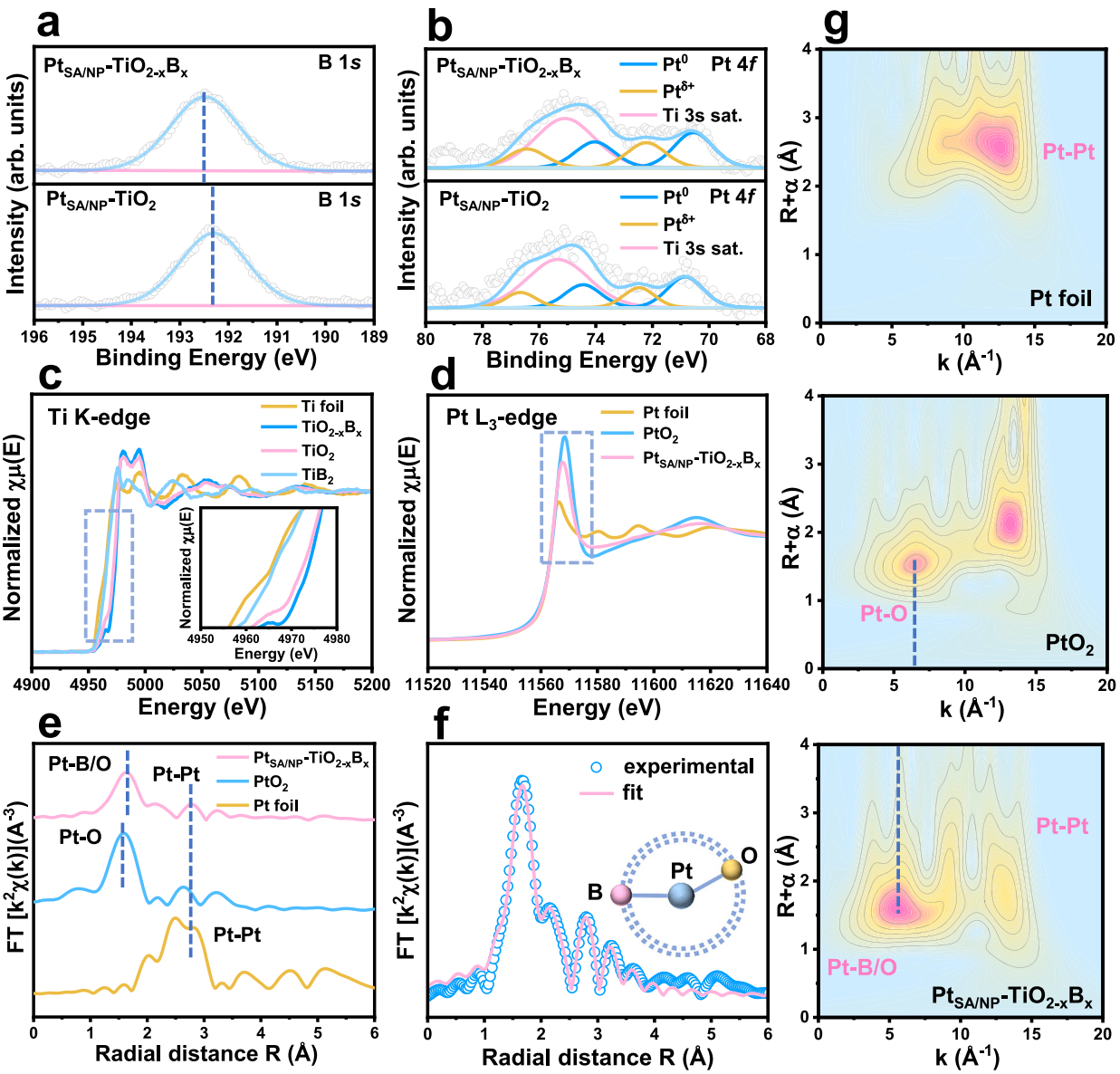

Fig. 3 | Electronic properties and local coordination environment of the photocatalysts. XPS spectra of **a** B 1*s* for $TiO_{2-x}B_x$ and $Pt_{SA/NP}$-$TiO_{2-x}B_x$. **b** Pt 4*f* for $Pt_{SA/NP}$-TiO_2 and $Pt_{SA/NP}$-$TiO_{2-x}B_x$. **c** normalized Ti K-edge XANES spectra of TiO_2, $TiO_{2-x}B_x$ and reference Ti foil and TiB_2. **d** normalized Pt L_3-edge XANES spectra and **e** FT-EXAFS spectra of $Pt_{SA/NP}$-$TiO_{2-x}B_x$ and reference Pt foil and PtO_2. **f** Pt L_3-edge fitted EXAFS spectra of R space for $Pt_{SA/NP}$-$TiO_{2-x}B_x$. **g** WT EXAFS contour plots for the k_3-weighted Pt L_3-edge EXAFS of Pt foil, PtO_2 and $Pt_{SA/NP}$-$TiO_{2-x}B_x$. R denotes the radial distance (Å) and k denotes the photoelectron wave vector (Å^{-1}) in XAFS analysis. Source data are provided as a Source Data file.

(Supplementary Fig. 15, CO adsorption on SA is directly proportional to the total SAs whereas NP is related only to the surface atoms[44,47]), the estimated atomic ratios of SA to NP in the $Pt_{SA/NP}$-TiO_2 and $Pt_{SA/NP}$-$TiO_{2-x}B_x$ are approximately 1:16 and 1:13, respectively. (for detailed discussion, refer to Supplementary Figs. 14 and 15). Elemental mapping (Fig. 2g) confirms the homogeneous distribution of B and Pt across the surface of the $Pt_{SA/NP}$-$TiO_{2-x}B_x$.

Atomic coordination structure analysis

To better elucidate the chemical states and the local coordination environment of Pt cocatalysts, X-ray Photoelectron Spectroscopy (XPS) and X-ray Absorption Fine Structure (XAFS) analyses were conducted. The full spectrum of the photocatalysts (Supplementary Fig. 16a) verifies the presence of B, O, and Ti in the samples, with no detectable impurity peaks. The absence of Pt signal in the full spectrum can be attributed to its low content. Inductively coupled plasma (ICP) analysis of the optimal $Pt_{SA/NP}$-$TiO_{2-x}B_x$ photocatalyst reveals that the contents of B and Pt are 1.56 wt.% and 0.37 wt.% (Supplementary Fig. 16b), respectively. XPS fine spectra were used to investigate the charge transfer dynamics between B and Pt. As shown in Fig. 3a, the B signal on $TiO_{2-x}B_x$ and $Pt_{SA/NP}$-$TiO_{2-x}B_x$ is directly detected. The binding energy of B 1*s* appears at 192 eV, suggesting that B exists in a doped substitutional state without other impurity species[37,43], consistent with the XRD results.

The Pt 4*f* fine spectrum (Fig. 3b) indicates that Ti 3*s* satellite peaks (~ 75 eV) overlap with Pt 4*f* peaks, complicating the deconvolution of Pt 4*f* curves for $Pt_{SA/NP}$-TiO_2 and $Pt_{SA/NP}$-$TiO_{2-x}B_x$[48]. During catalyst preparation, the Pt precursor (Pt^{4+}) is partially reduced to form $Pt^{\delta+}$ species

(Pt SA coordinated with the surface lattice O) and fully reduced to Pt^0 (metallic Pt NP)[49]. The peak area ratio of Pt $4f_{5/2}$ to $4f_{7/2}$ was strictly fixed at 3:4, and the full width at half maximum (FWHM) of all Pt^0 and $Pt^{\delta+}$ peaks was set uniformly during deconvolution[48,49]. In Fig. 3b, peaks at 70.84 and 74.41 eV are attributed to Pt^0 $4f_{7/2}$ and $4f_{5/2}$ signals of $Pt_{SA/NP}$-TiO_2, respectively, while peaks at 72.45 and 76.65 eV correspond to $Pt^{\delta+}$ $4f_{7/2}$ and $4f_{5/2}$ signals. According to the principles of XPS binding energy measurements (Supplementary Fig. 17a), changes in the local valence electron density can affect the binding energy shift through two opposing mechanisms: (1) through variations in screening effect of the nuclear charge[50] (Supplementary Fig. 17b, Mechanism 1), and (2) through Fermi level shifts associated with changes in carrier density[51] (Supplementary Fig. 17c, Mechanism 2). Mechanism 1, which reflects the direct shielding of the nucleus by valence electrons, exerts a more dominant influence on both the direction and magnitude of binding energy shifts than the Fermi-level related band position changes described in Mechanism 2, particularly in metal-oxide catalysts[49,50] (For more detailed discussion, refer to Supplementary Fig. 17). Based on this understanding, the observed increase in O 1*s* and Ti 2*p* binding energies of $Pt_{SA/NP}$-TiO_2 relative to pristine TiO_2 upon Pt loading (Supplementary Fig. 18) indicates a reduction in surface electron density, this electron depletion near the surface leads to the formation of upward band bending[52] (For more detailed discussion, refer to Supplementary Fig. 19).

The reduced binding energy of Pt 4*f* ($Pt^{0\prime}$: 70.63 and 74.07 eV; $Pt^{\delta\prime+}$: 72.24 and 76.37 eV) and further enhanced binding energy of the substrate elements (Ti, O, and B, Fig. 3a and Supplementary Fig. 18) for $Pt_{SA/NP}$-$TiO_{2-x}B_x$, as corroborated by the XPS results with different Pt and B contents (Supplementary Figs. 20 and 21), reflects more electrons transfer from the $TiO_{2-x}B_x$ substrate to Pt cocatalysts by B doping, resulting in the formation of $Pt^{\delta\prime+}$ and $Pt^{0\prime}$ species that are electron-rich and have a slightly lower valence state (For more detailed discussion on the valence state changes of the Pt species, refer to Supplementary Fig. 21), which further enhances electron depletion near the $Pt_{SA/NP}$-$TiO_{2-x}B_x$ surface, leading to a more pronounced upward band bending (Supplementary Fig. 19). Moreover, this electron enrichment in Pt sites is expected to increase the *5d* orbital occupation[53], which is considered to play a critical role in determining the catalytic activity, thereby influencing the binding interactions of Pt sites and reaction intermediates[54].

To further investigate the local coordination environment of Pt species in $Pt_{SA/NP}$-$TiO_{2-x}B_x$, element-selective XAFS measurements were performed. The Ti K-edge X-ray absorption near-edge structure (XANES) spectra show the absorption edge of $TiO_{2-x}B_x$ is located between that of TiO_2 and TiB_2 (Fig. 3c), and the k^2 weighted Fourier transform extended X-ray absorption fine structure (FT-EXAFS) reveals the longer bond length of $TiO_{2-x}B_x$ than TiO_2 (Supplementary Fig. 22), which further confirms that the B replaces O in $TiO_{2-x}B_x$ since the length of Ti-B bond is longer than Ti-O bond[43]. Notably, the Ti K-edge FT-EXAFS spectra show the shorter bond length of $TiO_{2-x}B_x$ than that of TiB_2 (Supplementary Fig. 22). This is reasonable, as only a small fraction of O atoms in $TiO_{2-x}B_x$ are replaced by B (contents of B is 1.56 wt.%), resulting in localized structural changes rather than the extensive bonding observed in TiB_2, which means the overall lattice integrity maintains well while introducing the targeted modifications.

The Pt L_3-edge XANES spectra reveal that $Pt_{SA/NP}$-$TiO_{2-x}B_x$ exhibits a lower white line intensity than PtO_2 but higher than Pt foil (Fig. 3d). This suggests that the Pt species in $Pt_{SA/NP}$-$TiO_{2-x}B_x$ possess a valence range between 0 to +4, consistent with the coexistence of Pt^0 and $Pt^{\delta+}$ states observed in the XPS results. FT-EXAFS spectral (Fig. 3e) analysis highlights the atomic dispersion of the Pt cocatalyst. Distinct features in the first and second coordination shells are observed: the signal around 2.2 Å in the second coordination shells corresponds to Pt-Pt bonds of Pt NPs. Notably, In the first coordination shell, the peak corresponding to Pt SAs resembles that of PtO_2 but with a bond length elongated by 0.08 Å, which can be attributed to the partial substitution of O by B to form P-B/O (B-P-O) bonds as the length of Pt-B bond (2.18 Å) is longer than Pt-O bond (2.02 Å)[38]. In addition, Supplementary Fig. 23a illustrates that the k-space scattering pathways of $Pt_{SA/NP}$-$TiO_{2-x}B_x$ diverge from those of PtO_2, reflecting a distinct Pt coordination environment in $Pt_{SA/NP}$-$TiO_{2-x}B_x$ relative to Pt-O. Based on the combined analysis of Raman, HAADF-STEM, XPS, and XAFS results, it can be inferred that Pt and B have respectively substituted for Ti and O in the TiO_2 lattice, leading to the formation of B-Pt bonds. The proposed formation mechanism of the asymmetric B-Pt-O coordination structure is illustrated in Supplementary Fig. 24.

EXAFS fitting (Fig. 3f, Supplementary Table 2) reveals a coordination model involving Pt-O, Pt-B, and Pt-Pt structures. The fitted Pt-B coordination number of 1.5 suggests that one or two O atoms coordinated with Pt are replaced by B atoms, forming B-P-O motifs. Wavelet transform (WT) analysis provides further evidence for the Pt-B/O configuration. The WT intensity maxima for $Pt_{SA/NP}$-$TiO_{2-x}B_x$ appears at R+α = 1.6 Å, shifting to lower k-values compared to PtO_2 standards, indicating coordination between Pt and lighter atoms[55], specifically B. Additionally, an intensity maximum at R+α = 2.2 Å can be observed, corresponding to the Pt-Pt coordination of the Pt NPs. The substantial electronegativity disparity between B and O facilitates the electron redistribution between B-Pt and O-Pt bonds within the B-P-O coordination, resulting in asymmetric electron density distribution. This further facilitates the electron transfer from the TiO_2 to Pt cocatalysts, consistent with the XPS results.

Evaluation of photocatalytic activity

To evaluate the performance of the photocatalyst in water-splitting reactions, methanol served as a sacrificial agent, and the H_2 evolution rate was monitored under 365 nm. As shown in Fig. 4a, pristine TiO_2 generates H_2 of 2.73 mmol $g^{-1}h^{-1}$, while $TiO_{2-x}B_x$ exhibits a roughly sevenfold enhancement in PHE (10.31 mmol $g^{-1}h^{-1}$). Furthermore, the modification of Pt SAs and NPs yielded $Pt_{SA/NP}$-TiO_2 photocatalyst with an enhanced PHE rate of 214.3 mmol $g^{-1}h^{-1}$ and AQE of 54.7%, which can be attributed to the high intrinsic activity of Pt cocatalysts and the synergistic effect between Pt SAs and NPs for HER[15]. Notably, B doping further elevates the PHE rate of $Pt_{SA/NP}$-$TiO_{2-x}B_x$ to 627.6 mmol $g^{-1}h^{-1}$, representing 60.1-fold and 2.9-fold improvements over TiO_{2-x} and $Pt_{SA/NP}$-TiO_2, respectively, with an AQE of 98.4 % at 365 nm, nearing the theoretical maximum of unity (Fig. 4b and Supplementary Table 3). The TOF of $Pt_{SA/NP}$-$TiO_{2-x}B_x$ is calculated to be 33090 h^{-1} (Supplementary Table 3), which is three times higher than that of $Pt_{SA/NP}$-TiO_2 (10197 h^{-1}). This notable photocatalytic performance is also evidenced by the continuous H_2 bubble formation on the $Pt_{SA/NP}$-$TiO_{2-x}B_x$ catalysts surface under irradiation (Supplementary Movie 1). To exclude the differences in Pt content due to B doping contributed to the observed PHE variations, the PHE rates of $Pt_{SA/NP}$-$TiO_{2-x}B_x$ and $Pt_{SA/NP}$-TiO_2 were compared with different Pt content. As shown in Fig. 4c, $Pt_{SA/NP}$-$TiO_{2-x}B_x$ consistently exhibits higher PHE than $Pt_{SA/NP}$-TiO_2 across all levels of Pt content and varying wavelengths (Supplementary Fig. 25), and the optimal PHE rate of $Pt_{SA/NP}$-$TiO_{2-x}B_x$ is achieved with 0.4 wt.% Pt and 3 wt.% B (Supplementary Figs. 26 and 27). Coupled with the competitive performance evidenced in Fig. 4d, these results verify that B doping is the primary factor driving the enhancement in PHE activity. To confirm the synergy of SA and NP in the PHE reaction, Pt_{SA}-$TiO_{2-x}B_x$ and Pt_{NP}-$TiO_{2-x}B_x$ photocatalysts containing only SA and only NP were synthesized (Fig.2f, Supplementary Figs. 11 and 12) and evaluated the photocatalytic performance, respectively. The optimal Pt_{SA}-$TiO_{2-x}B_x$ and Pt_{NP}-$TiO_{2-x}B_x$ samples exhibit PHE rates of 136.7 and 302.7 mmol $g^{-1}h^{-1}$ (Supplementary Fig. 28), respectively, with corresponding TOF values of 14815 and 5789 h^{-1} (Supplementary Fig. 29), both of which were lower than those of $Pt_{SA/NP}$-$TiO_{2-x}B_x$, confirming the synergistic effect between SA and NP in enhancing HER performance.

https://doi.org/10.1038/s41467-025-63637-2

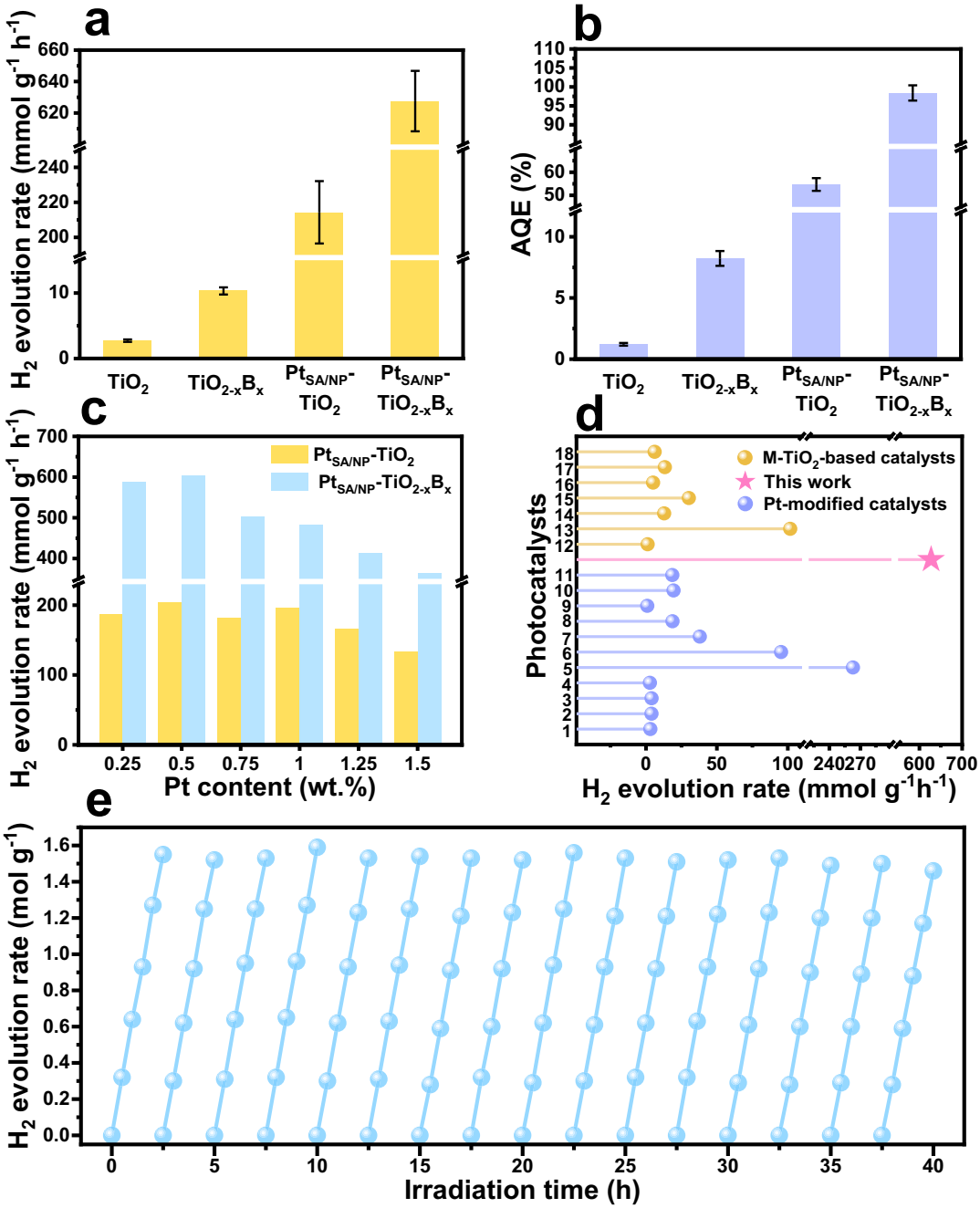

Fig. 4 | PHE activity evaluation of the photocatalysts at 40 °C. a Photocatalytic H_2 evolution rates and **b** AQE for H_2 evolution of the photocatalysts, the error bars are defined as standard deviation, and the center of each error bar represents the mean of three independent measurements ($n = 3$). **c** Photocatalytic H_2 evolution rates of $Pt_{SA/NP}$-TiO_2 and $Pt_{SA/NP}$-$TiO_{2-x}B_x$ with different Pt content. **d** The PHE summary of the previously reported Pt-modified-photocatalysts and M-TiO_2-based (M stands for metal) photocatalysts (reaction temperature ≥ 40 °C), the numbered data of photocatalysts are as follows: 1) Pt(1.0%)/TiO_2, 2) Cu(0.01%)/Pt(1.0%)/TiO_2, 3) Ni(0.01%)/Pt(1.0%)/TiO_2, 4) Pd(0.01%)/Pt(1.0%)/TiO_2, 5) PtCu-TiO_2, 6) PtSA-TiO_2, 7) Pt/TiO_2-101, 8) 1 wt %Pt-TiO_2, 9) 1 wt% Pt-g-C_3N_4, 10) 1%Pt/ZIS, 11) 1%Pt-TiO_2, 12) 1% Ag/TiO_2, 13) CuSA-TiO_2, 14) 1%Au-1%Ag/TiO_2, 15) Ag@SiO_2@TiO_2NS/Au, 16) Rh/TiO_2, 17) 1%Au/TiO_2, 18) In_{SA}/TiO_2. (summarized in detail in Supplementary Table 6). **e** PHE cycling stability of $Pt_{SA/NP}$-$TiO_{2-x}B_x$. Source data are provided as a Source Data file.

The PHE rates of $Pt_{SA/NP}$-$TiO_{2-x}B_x$ with different methanol/water ratios are shown in Supplementary Fig. 30, highlighting the advantage of a 66.7% methanol proportion in enhancing photocatalytic H_2 evolution. Isotope experiments were conducted by replacing water and methanol with heavy water (D_2O) and deuterated methanol (CD_3OD) with same ratio, respectively, proving water is the primary hydrogen source of photocatalytic H_2 evolution (for more detailed discussion, refer to Supplementary Fig. 31). In addition, infrared thermograms during the photocatalytic reaction process and the PHE rates at different temperatures (20–70 °C) are presented in Supplementary Figs. 28 and 29, revealing the advantages of photocatalytic reaction under 40 °C. (For more detailed discussion, refer to Supplementary Figs. 32 and 33).

Furthermore, to verify the importance of B-Pt-O coordination for photocatalytic H_2 evolution, a control sample $Pt_{SA/NP}$@$TiO_{2-x}B_x$ (contains B doping and P loading but without B-P coordination) was

synthesized and compared with $Pt_{SA/NP}$-$TiO_{2-x}B_x$. HAADF-STEM (Supplementary Fig. 34) imaging confirmed the coexistence of Pt SA and NP in $Pt_{SA/NP}$@$TiO_{2-x}B_x$, while XPS (Supplementary Fig. 35) and XAFS (Supplementary Fig. 36) analyses verified the exclusive presence of Pt-O coordination without Pt-B bonding (for more details, please refer to Supplementary Figs. 35 and 36, and Supplementary Table 4). The optimized $Pt_{SA/NP}$@$TiO_{2-x}B_x$ sample exhibits a lower PHE rate of 335.4 mmol $g^{-1}h^{-1}$ (Supplementary Fig. 37) compared to $Pt_{SA/NP}$-$TiO_{2-x}B_x$, further confirming the critical role of B-Pt-O coordination in promoting photocatalytic H_2 evolution.

Further comparisons with various metal cocatalysts of equivalent content reveal that B-doped M-TiO_2 (M: Ag, Ru, Ir, Cu, Fe, Co, Ni, Zn) photocatalysts exhibit discrepant PHE rates (Supplementary Fig. 38), with Pt cocatalysts standing out due to its high intrinsic activity and the enhanced synergistic effects between Pt SAs and NPs facilitated by B doping. Long-term stability measurements conducted during cyclic water-splitting experiments show that the PHE rate remains stable over 40 hours (Fig. 4e). Post-reaction structural analysis using XRD, TEM, and HAADF-STEM further verify the stability of $Pt_{SA/NP}$-$TiO_{2-x}B_x$ (Supplementary Fig. 39). The crystalline structure and surface lattice morphology of $Pt_{SA/NP}$-$TiO_{2-x}B_x$ show no observable changes compared to the pre-reaction samples (Supplementary Fig. 39a-c). Line scan profiles and HAADF-STEM analysis confirm that Pt SAs remain well-dispersed on TiO_2 (Supplementary Fig. 39d-e), with no observable agglomeration of Pt SAs or changes in the grain size of Pt NPs (Supplementary Fig. 39f). The element mapping also confirms the remaining dispersion of B and Pt after the photocatalytic reaction (Supplementary Fig. 39g). These analyses demonstrate the stability and strong anchoring of Pt SAs with B-Pt-O coordination on the TiO_2 support, attributable to the porosity and unsaturated bonding of the MIL-125(Ti_V) framework, which effectively stabilizes Pt cocatalysts.

Charge transfer-separation efficiency of the photocatalysts

Photocatalysts Ultraviolet-visible (UV-vis) spectroscopy was employed to analyze the light absorption properties of the photocatalysts. As shown in Fig. 5a, $Pt_{SA/NP}$-TiO_2 and $Pt_{SA/NP}$-$TiO_{2-x}B_x$ exhibit stronger absorption intensities beyond 400 nm compared to TiO_2 and $TiO_{2-x}B_x$, attributed to the darkened colouration of the catalysts induced by Pt NPs. Furthermore, the red-shifted absorption edges observed for $TiO_{2-x}B_x$ and $Pt_{SA/NP}$-$TiO_{2-x}B_x$, compared to TiO_2 and $Pt_{SA/NP}$-TiO_2, suggest that B doping effectively narrows the bandgap of TiO_2. The Tauc plots further corroborate this (Fig. 5b). The calculated energy band positions from XPS valence band spectra (Supplementary Fig. 40), as depicted in Supplementary Fig. 41, indicate that $TiO_{2-x}B_x$ and $Pt_{SA/NP}$-$TiO_{2-x}B_x$ exhibit narrower bandgaps, and the estimated positions of the conduction band minimum (CBM) and valence band maximum (VBM) of $Pt_{SA/NP}$-TiO_2 and $Pt_{SA/NP}$-$TiO_{2-x}B_x$ both moved upward, which is consistent with the XPS analysis of the upward band bending (Supplementary Fig. 19). These findings conform to the result that $Pt_{SA/NP}$-$TiO_{2-x}B_x$ exhibits higher PHE efficiency under various wavelengths than $Pt_{SA/NP}$-TiO_2.

Figure 5c presents the magnetic moment versus magnetic field (M-H) curves for TiO_2, $Pt_{SA/NP}$-TiO_2, and $Pt_{SA/NP}$-$TiO_{2-x}B_x$ catalysts, measured in a magnetic field range from −3 to 3 T at 300 K. It can be seen that TiO_2 exhibits a typical M-H curve with a saturation magnetization of 0.011 emu g^{-1}, which is consistent with the previous reports[56]. In contrast, both $Pt_{SA/NP}$-TiO_2 and $Pt_{SA/NP}$-$TiO_{2-x}B_x$ show significantly improved saturation magnetization compared to TiO_2, attributed to the changes in electronic structure induced by the two-dimensional quantum confinement effect from Pt species, particularly the enhanced spin polarization[57,58]. Furthermore, $Pt_{SA/NP}$-$TiO_{2-x}B_x$ exhibits a higher saturation magnetization (0.024 emu g^{-1}) than $Pt_{SA/NP}$-TiO_2 (0.020 emu g^{-1}), suggesting that the B-Pt-O asymmetric coordination further strengthens the spin polarization of Pt. The disparity between spin-up and spin-down charge densities caused by spin polarization can enhance the charge separation[59].

To investigate the carrier dynamics associated with the potential B-Pt-O interfacial sites, the photocurrent response and electrochemical impedance spectroscopy (EIS) were performed. The results indicate that the $Pt_{SA/NP}$-$TiO_{2-x}B_x$ photocatalyst demonstrates the highest photocurrent density (Fig. 5d) and the smallest EIS semicircular radius (Fig. 5e) in the four samples, which can be attributed to the improved charge separation efficiency and reduced interfacial charge transfer resistance. Additionally, the $Pt_{SA/NP}$-$TiO_{2-x}B_x$ photocatalyst shows notable stability and reproducibility, maintaining consistent photocurrent response over 10 on-off cycles. Photoluminescence (PL) and Time-Resolved PL (TRPL) results further substantiate the role of B in promoting charge carrier separation and transfer. As illustrated in Fig. 5f, pristine TiO_2 exhibits a high PL intensity due to the significant charge carrier recombination and slow charge transfer. Upon introduction of B and Pt, $Pt_{SA/NP}$-$TiO_{2-x}B_x$ exhibits a significant reduction in PL intensity, signifying the suppression of photogenerated electron-hole recombination. TRPL lifetime directly reflects the overall decay rate of singlet excitons and involves two competing processes: radiative recombination (fluorescence emission) or non-radiative transfer (exciton dissociation)[60]. Based on the fact of effective carrier separation confirmed by photocurrent and EIS results, the shortened lifetime of $Pt_{SA/NP}$-$TiO_{2-x}B_x$ (Fig. 5g and Supplementary Table 5) suggests enhanced surface-mediated exciton dissociation of non-radiative processes, where photogenerated electrons and holes are rapidly captured by Pt species and the $TiO_{2-x}B_x$ substrate[61,62], respectively, which can be attributed to the B-Pt-O interfacial electric field. These findings highlight the role of B-Pt-O units in enhancing photocatalytic performance by promoting efficient charge carrier dynamics.

The separation and transfer of photogenerated carriers is a complex process of multiple time and space scales[63], thus, electron transfer mechanisms of $Pt_{SA/NP}$-TiO_2 and $Pt_{SA/NP}$-$TiO_{2-x}B_x$ during photocatalysis were studied using surface photovoltage (SPV), in-situ irradiated XPS (ISI-XPS) and in-situ irradiated Electron Paramagnetic Resonance (EPR) analysis. The SPV of the samples was measured using a Kelvin probe system (Supplementary Fig. 42), which is rigidly defined as the illumination-induced changes in the surface potential (V_s), and it is directly related to the initial transient separation of photogenerated charge carriers by the built-in electric field in the space charge region (SCR)[52,64]. Under dark conditions, $Pt_{SA/NP}$-TiO_2 and $Pt_{SA/NP}$-$TiO_{2-x}B_x$ exhibit V_s of ~ −30 mV and ~ −71 mV, respectively, indicating the $Pt_{SA/NP}$-$TiO_{2-x}B_x$ sample shows a more pronounced band bending. Upon illumination, as the light intensity increases, the V_s eventually stabilizes at a constant positive value ($Pt_{SA/NP}$-TiO_2 for ~54 mV and $Pt_{SA/NP}$-$TiO_{2-x}B_x$ for ~43 mV), indicating that the surface band bending has approached complete flattening[64] (For more detailed discussion, refer to Supplementary Figs. 43 and 44 in Supplementary Information). This steady-state value corresponds to the saturated surface photovoltage (SPV_{sat})[52]. Previous studies have established that a positive SPV value corresponds to upward band bending, and the magnitude of the SPV_{sat} value reflects the extent of band bending[65]. As shown in Supplementary Fig. 42, $Pt_{SA/NP}$-TiO_2 and $Pt_{SA/NP}$-$TiO_{2-x}B_x$ exhibit SPV_{sat} of ~ 84.4 mV and ~ 114.6 mV, respectively. This indicates that the upward surface band bending for the two samples, and that the band bending is more pronounced in the $Pt_{SA/NP}$-$TiO_{2-x}B_x$. These observations are consistent with the XPS analysis presented above.

ISI-XPS offers an approach for probing the electron transfer pathways during the photocatalytic process, which reflects the steady-state electronic structure that emerges after prolonged light exposure[66]. Figure 6a–c and Supplementary Fig. 45 exhibit a decreased binding energy in the $Pt^{\delta+}$ 4*f* and an increase in the substrate elements (Ti 2*p*, O 1*s*, and B 1*s*) under 30 minutes of continuous illumination,

https://doi.org/10.1038/s41467-025-63637-2

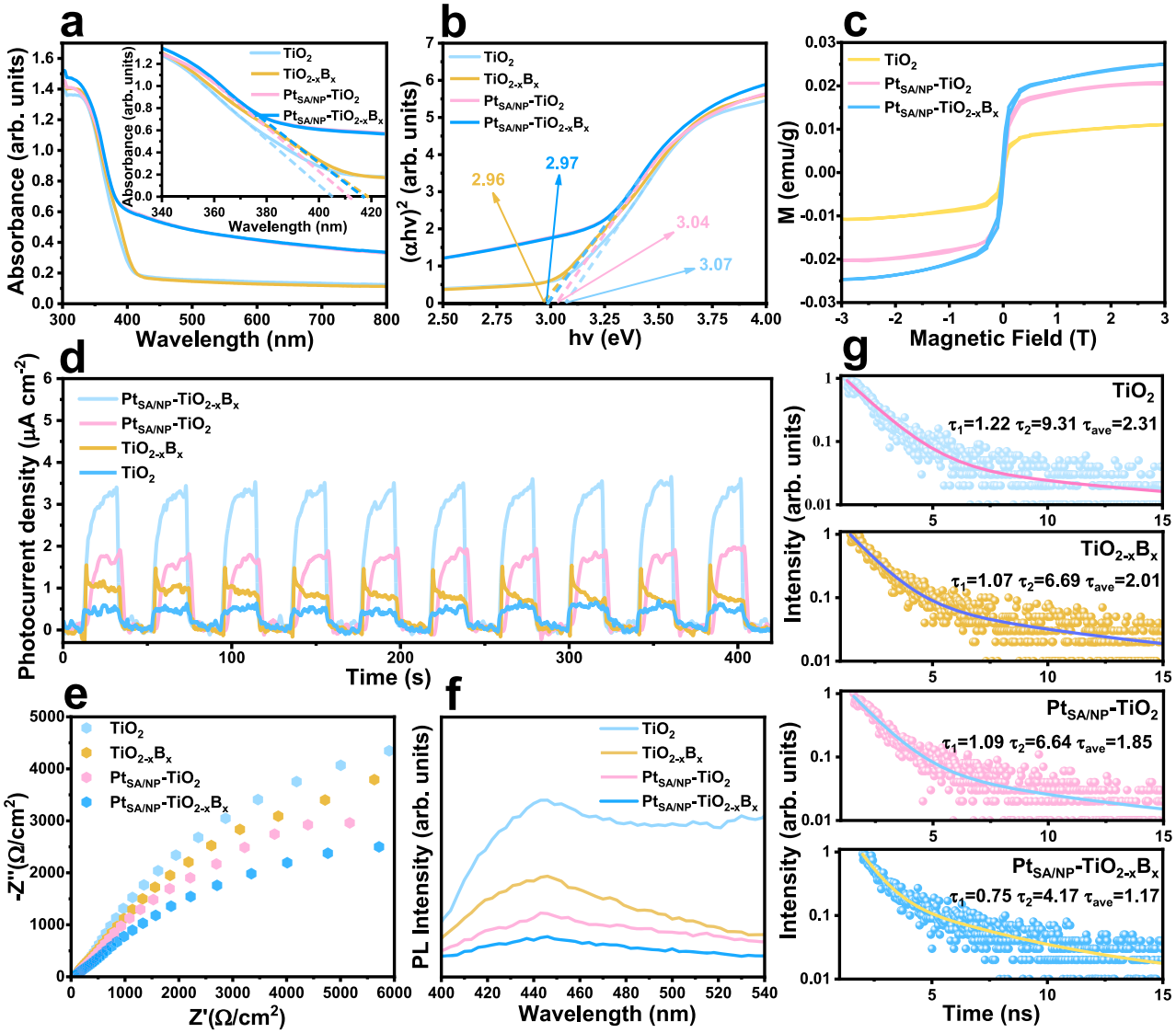

Fig. 5 | Carrier dynamics and energy band structure of the photocatalysts. a UV-vis spectra and **b** Tauc diagrams converted from UV-vis of TiO_2, $TiO_{2-x}B_x$, $Pt_{SA/NP}$-TiO_2 and $Pt_{SA/NP}$-$TiO_{2-x}B_x$. **c** M-H hysteresis of TiO_2, $Pt_{SA/NP}$-TiO_2 and $Pt_{SA/NP}$-$TiO_{2-x}B_x$. **d** Transient photocurrent responses and **e** EIS plots of TiO_2, $TiO_{2-x}B_x$, $Pt_{SA/NP}$-TiO_2 and $Pt_{SA/NP}$-$TiO_{2-x}B_x$. **f** PL and **g** TRPL spectra of the photocatalysts. Source data are provided as a Source Data file.

indicating that photogenerated electrons transfer to Pt sites while photogenerated holes migrate toward the TiO_2 substrate. The shift in the $Pt^{\delta+}$ 4*f* binding energy under illumination is greater for $Pt_{SA/NP}$-$TiO_{2-x}B_x$ (0.32–0.41 eV) than for $Pt_{SA/NP}$-TiO_2 (0.19–0.24 eV). This further confirms that B-Pt-O coordination structure promots more efficient photogenerated electron transfer from the $TiO_{2-x}B_x$ substrate to the Pt active sites under light irradiation, which further disrupts the equilibrium charge distribution within SCR, inducing stronger upward band bending.

Therefore, by combining SPV and ISI-XPS analyses, the mechanism of carrier separation and transfer under illumination can be effectively elucidated, as well as the corresponding changes in the surface band structure (Supplementary Fig. 46). At the onset of illumination, photogenerated electron-hole pairs are generated within the SCR, leading to a temporary flattening of the upward band bending, as revealed by SPV measurements. As illumination continues, photogenerated electrons are transferred to the Pt active sites while photogenerated holes accumulate on the TiO_2 substrate, further disrupting the equilibrium charge distribution within SCR. This process leads to the re-establishment of a more pronounced upward band bending, as evidenced by ISI-XPS.

In-situ irradiated EPR measurements provide further evidence for this. As shown in Supplementary Fig. 47, $Pt_{SA/NP}$-TiO_2 exhibits a prominent signal for the O vacancy (O_V) at $g = 2.002$ under dark conditions. In contrast, the signal shifts to $g = 2.005$ in $Pt_{SA/NP}$-$TiO_{2-x}B_x$, which is attributed to the defect states introduced by B doping, including more O_V and the covalent $[BTi_3]$• structure[43]. Upon irradiation, both $Pt_{SA/NP}$-TiO_2 and $Pt_{SA/NP}$-$TiO_{2-x}B_x$ exhibit a weak EPR signal at $g = 2.01$, corresponding to the $Ti^{4+}O^{2-}Ti^{4+}O^{\bullet-}$ units[67]. This structure acts as a hole-trapping site, stabilizing photogenerated holes and reducing their free transfer, thus slowing the recombination between photogenerated holes and electrons at the interface[68]. Notably, the EPR signal at $g = 2.005$ in $Pt_{SA/NP}$-$TiO_{2-x}B_x$ is enhanced during irradiation and returns to its original state once the light source is removed. This

https://doi.org/10.1038/s41467-025-63637-2

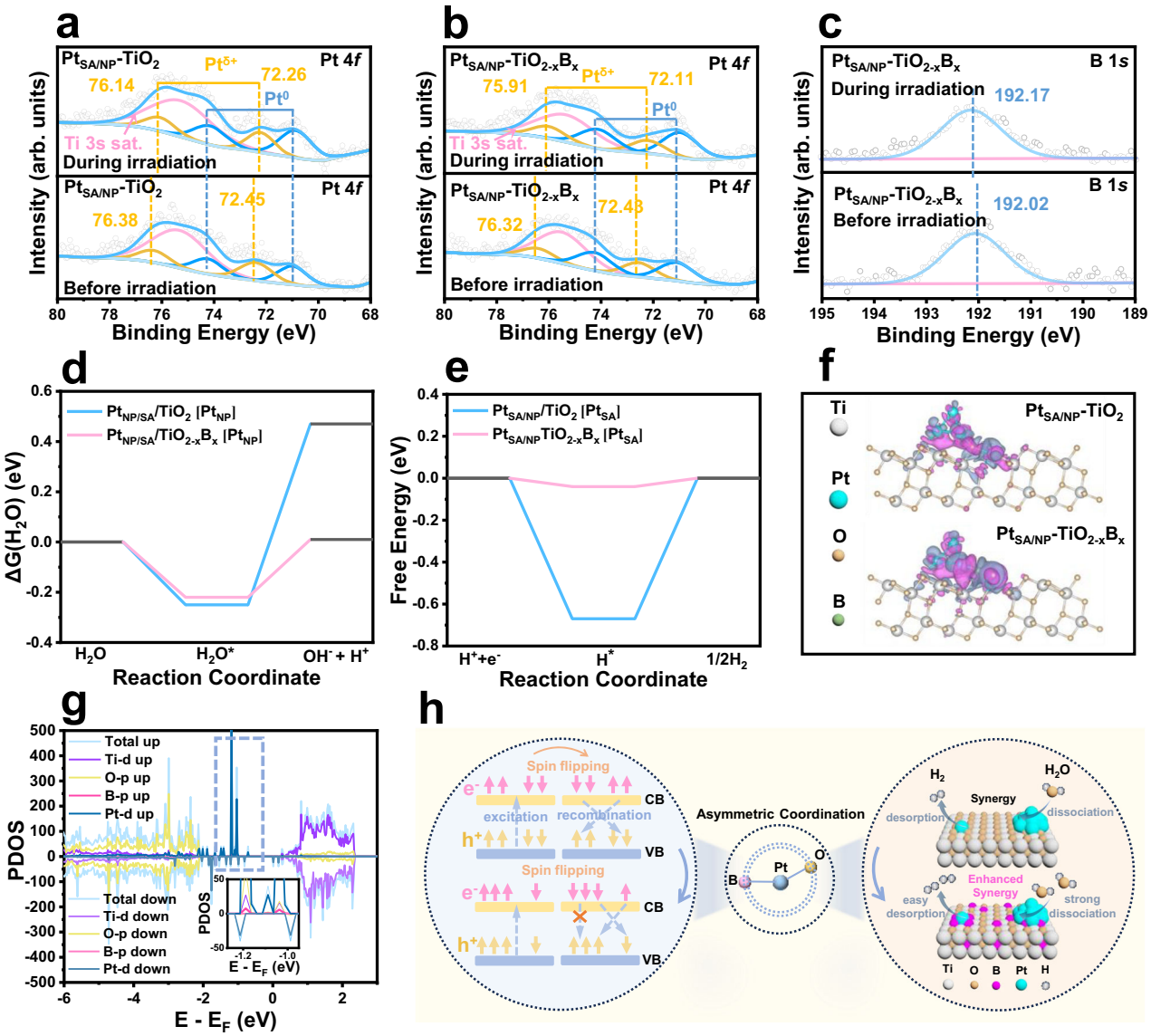

Fig. 6 | Photocatalytic mechanism and DFT calculation results. ISI-XPS for **a** Pt 4*f* of Pt$_{SA/NP}$-TiO$_2$, **b** Pt 4*f* of Pt$_{SA/NP}$-TiO$_{2-x}$B$_x$ and **c** B 1*s* of Pt$_{SA/NP}$-TiO$_{2-x}$B$_x$. **d** Free energy diagrams for the water-dissociation process for Pt NPs and **e** Hydrogen adsorption for Pt SAs over the Pt$_{SA/NP}$-TiO$_2$ and Pt$_{SA/NP}$-TiO$_{2-x}$B$_x$. **f** Charge density difference maps of Pt$_{SA/NP}$-TiO$_2$ and Pt$_{SA/NP}$-TiO$_{2-x}$B$_x$. Electron accumulation is purple, and depletion is gray, and the green, cyan, white and yellow spheres depict the B, Pt, Ti and O atoms, respectively. **g** Project density of states for Pt$_{SA/NP}$-TiO$_{2-x}$B$_x$. **h** Mechanism of spin polarization for improved charge separation and synergistic PHE over the Pt$_{SA/NP}$-TiO$_2$ and Pt$_{SA/NP}$-TiO$_{2-x}$B$_x$ photocatalysts. Source data are provided as a Source Data file.

demonstrates an increase in the number of unpaired electrons during illumination, further verifying that the transfer of photogenerated electrons can be promoted by B doping.

Mechanistic insights into the asymmetric coordination

Density functional theory (DFT) calculations have been performed to gain detailed and deep insights into the roles of the B-Pt-O coordination on the Pt-SA/NP dual sites. Both Pt SA and NP were placed in adjacent positions on the TiO$_2$ surface, with B atoms substituted for O atoms and identified as stable structure (Supplementary Fig. 48). B atoms coordinated with Pt SA to form a stable 2-coordinate structure, as confirmed by the XAFS fitting results. Pt NP and SA were identified as the H_2O activation and H_2 desorption sites during model optimization, respectively, which aligns with ISI-XPS results and previous reports[14,21]. Therefore, the role of B can be determined by directly comparing the dissociation of H_2O* at the Pt NP sites, along with the adsorption-desorption of H* at the Pt SA sites in Pt$_{SA/NP}$-TiO$_2$ and Pt$_{SA/NP}$-TiO$_{2-x}$B$_x$ catalysts. In the water-splitting reactions, the dissociation of H_2O molecules through the cleavage of the covalent HO-H bond is a critical and rate-limiting step. Figure 6d shows the optimized configurations of H_2O, H_2O*, and OH^- + H* at the NP sites. H_2O molecules are stably adsorbed at the Pt NP sites of both Pt$_{SA/NP}$-TiO$_2$ and Pt$_{SA/NP}$-TiO$_{2-x}$B$_x$, forming a transition state of H_2O*. However, the dissociation of H_2O* into OH^- + H* shows a more pronounced uphill process on Pt$_{SA/NP}$-TiO$_2$ compared to Pt$_{SA/NP}$-TiO$_{2-x}$B$_x$. Specifically, at the Pt NP site, the energy barrier for H_2O* dissociation is 0.72 eV for Pt$_{SA/NP}$-TiO$_2$ and 0.23 eV for Pt$_{SA/NP}$-TiO$_{2-x}$B$_x$, indicating that B doping efficiently enhances the dissociation of H_2O molecules. Additionally, the Gibbs free energy of H* adsorption/desorption is −0.67 eV for Pt-SA in Pt$_{SA/NP}$-TiO$_{2-x}$B$_x$ and −0.04 eV in Pt$_{SA/NP}$-TiO$_{2-x}$B$_x$ (Fig. 6e), suggesting the easier H* desorption on Pt-SA of Pt$_{SA/NP}$-TiO$_{2-x}$B$_x$ than on Pt$_{SA/NP}$-TiO$_2$, where the adsorption/desorption process is closer to equilibrium. These results

demonstrate that B enhances the synergy between the dual sites, facilitating both the H_2O^* dissociation at the Pt NP and H* desorption at the Pt SA.

According to molecular orbital theory, the interaction between the H* intermediate and the Pt active site is governed by orbital coupling between the H 1*s* orbital and the Pt 5*d* orbital (Pt-H_{ads}), leading to the formation of bonding and antibonding states. The electronic occupation of the Pt site determines the anti-bonding orbital filling of Pt-H_{ads}, thereby influencing the catalytic activity[53]. However, due to strong interactions between Pt atoms and the TiO_2, electrons tend to transfer from the Pt sites to the TiO_2 substrate, creating electron-deficient Pt centers, which strengthens the Pt-H_{ads} bond[69], hindering the desorption of adsorbed H* and ultimately suppressing photocatalytic H_2 evolution (Supplementary Fig. 49). This issue was alleviated by constructing the B-Pt-O asymmetric coordination through B doping, the charge density difference maps (Fig. 6f) reveal an asymmetric distribution of electron density on the Pt species, with more localized electron density at Pt sites of $Pt_{SA/NP}$-$TiO_{2-x}B_x$, suggesting the enhanced MSI for promoting the electron transfer from $TiO_{2-x}B_x$ substrate to Pt sites and enriches the Pt 5*d* orbitals filling (consistent with the XPS results), increasing the occupation of the antibonding orbitals in the Pt-H_{ads}. Therefore, the Pt-H_{ads} bond strength is weakened, lowering the H* adsorption energy and facilitating the desorption of H* from the Pt active sites[53,70] (Supplementary Fig. 49). This modulation of the electronic structure thus enhances the photocatalytic H_2 evolution performance.

To understand the factors influencing the synergy, the project density of states (PDOS) of catalysts were analyzed. Figure 6g and Supplementary Fig. 50 illustrate the PDOS of $Pt_{SA/NP}$-$TiO_{2-x}B_x$ and $Pt_{SA/NP}$-TiO_2 photocatalysts. Obviously, the conduction band (CB) and valence band (VB) are primarily derived from Ti 3 *d* and O 2*p* orbitals, respectively. The introduction of B narrows the band gap of TiO_2 (2.60 eV of $Pt_{SA/NP}$-TiO_2 and 2.47 eV of $Pt_{SA/NP}$-$TiO_{2-x}B_x$), consistent with the above UV-Vis results (Fig. 5a). Additionally, a spin-up density of states of Pt-*d* up near the Fermi level in $Pt_{SA/NP}$-TiO_2 can be observed (Supplementary Fig. 50), primarily ascribed to the hybridization of the *d*-*p* orbitals of Pt and O, which leads to a spin-polarized electron alignment, consistent with the M-H results. Notably, the spin-up state density of Pt-*d* up in $Pt_{SA/NP}$-$TiO_{2-x}B_x$ (Fig. 6g) is much higher than $Pt_{SA/NP}$-TiO_2 (Supplementary Fig. 50) due to the changed *d*-*p* orbital hybridization of Pt and B/O. This suggests the asymmetric B-Pt-O coordination disturbs the balance between spin-up and spin-down electrons of Pt, resulting in electron polarization and increasing the availability of spin-up electrons, disclosing its efficient charge separation. The associated mechanism is illuminated (Fig. 6h) to elucidate the impact of spin polarization on charge separation. Under light irradiation, spin-up electrons are excited into the CBM while the corresponding spin-up holes remain in the VBM. Due to the spin-orbit coupling (SOC) and hyperfine interactions (HFI), the excited spin-up electrons flip to spin-down while the spin-up holes maintain their orientation[59]. However, some of the holes with the opposite spin state can still recombine spontaneously with the flipped electrons. Stemming from the asymmetric coordination structure disturbs the balance between spin-up and spin-down electrons to increase the ratio of spin-up electrons, resulting in more spin-mismatched electrons and holes after the spin flipping, which helps suppress charge recombination[71]. This illustrates that higher spin polarization caused by the B-Pt-O asymmetric coordination enhances charge separation, which is consistent with the above PL results (Fig. 5f).

Therefore, the introduction of B enhances the efficiency of PHE through two main mechanisms: surface reactions and charge separation. First, B doping strengthens the MSI, facilitating the transfer of electrons from TiO_2 to the Pt species. The B-Pt-O asymmetric coordination structure leads to a redistribution of electron density between Pt SAs and NPs, influencing the dissociation and desorption of reactants at the dual sites, thereby optimizing the H_2 evolution reaction by water splitting. Second, the B-Pt-O asymmetric coordination disrupts the balance between spin-up and spin-down electrons on the Pt species, leading to increased spin polarization and more spin-up electrons. This promotes the charge carrier separation and suppresses the recombination. As a result, the synergy between the Pt SAs and NPs is enhanced to boost the PHE reaction (Fig. 6h).

In summary, the B-doped photocatalysts featuring the co-existence of Pt SAs and NPs were successfully synthesized by anchoring Pt species in Ti_V-containing MOF precursors and combining with a B-containing ligand substitution strategy. The optimal $Pt_{SA/NP}$-$TiO_{2-x}B_x$ photocatalyst exhibits notable photocatalytic performance (PHE rate for 627.6 mmol $g^{-1}h^{-1}$, AQE for 98.4%, and TOF value for 33090 h^{-1}), all of which are higher than that of the B-free counterpart. The experimental results confirmed that B doping modified the morphology and enhanced the light absorption of the photocatalyst. XAFS spectroscopy confirms the presence of B-P-O asymmetric coordination in $Pt_{SA/NP}$-$TiO_{2-x}B_x$, which enhances the MSI and promotes charge carrier separation and transport. In-situ characterization and theoretical analysis revealed that the B-Pt-O asymmetric coordination structure leads to a redistribution of electron density between Pt SAs and NPs, optimizing the adsorption-dissociation of the key intermediate H_2O^* by Pt NPs, as well as the adsorption-desorption of H* by Pt SAs, thus enhances the synergistic effect between Pt SAs and NPs. The findings highlight the importance of constructing asymmetric coordination through the introduction of heteroatoms to facilitate photogenerated carrier transfer and surface reactions. This design approach may be applied to other cocatalyst-semiconductor photocatalytic systems.

Methods

Materials and reagents

4-Carboxyphenylboronic acid (4-PBA acid, ≥97%), Titanium butoxide (TBOT, ≥99%), 1,4-benzenedicarboxylic acid (PTA, ≥99%), N, N-Dimethylformamide (DMF, ≥99.5%), Chloroplatinic acid (H_2PtCl_6, ≥99%), Na_2SO_4 (≥99.0%), methanol (≥99.5%) and ethanol (≥99.5%) were provided by Alad. Chem. RT Co. Ltd, (China).

Preparation of MOF B-MIL-125(Ti_V) precursor

The Ti-vacancy-containing MOF precursor, MIL-125(Ti_V), was synthesized via a modified solvothermal which adjustments to the titanium precursor amount to introduce Ti vacancies[10]. In a typical preparation, PTA (3.0 g) was dispersed in DMF (54 mL) and magnetically stirred for 15 min at ambient temperature. Methanol (6 mL) was then introduced into the suspension, followed by the dropwise addition of TBOT (1.25 mL, reduced from 1.56 mL reported in the literature[10]) under continuous stirring for 10 min. The resulting mixture was transferred into a 100 mL Schlenk tube, sealed, and heated at 130 °C for 20 h. After naturally cooling to room temperature, the solid product was collected by centrifugation, sequentially washed with DMF and methanol, and then dried under vacuum to remove residual solvents.

To fabricate B-MIL-125(Ti_V), a ligand substitution strategy was employed. Specifically, 0.5 g of 4-Carboxyphenylboronic acid was dissolved in 45 mL of DMF and stirred for 10 minutes. Subsequently, 5 mL of methanol and 1 g of MIL-125(Ti_V) were added to the solution, and ultrasonic treatment was applied to ensure thorough dispersion of the MIL-125(Ti_V). The mixture underwent a hydrothermal treatment at 130 °C for 20 hours, facilitating the ligand substitution process. The final product was then washed and dried to obtain the B-MIL-125(Ti_V).

Preparation of $Pt_{SA/NP}$-$TiO_{2-x}B_x$ and $Pt_{SA/NP}$-TiO_2

Typically, 0.3 g of B-MIL-125(Ti_V) was dispersed in 30 mL of deionized (DI) water. A specific amount of H_2PtCl_6 (e.g., 2.76 mg for 0.35 wt.% Pt) was then added to the suspension and stirred for 12 hours to facilitate

the synthesis of the encapsulated precursor. The resulting B-MIL-125(Pt) was centrifuged, washed with water, and dried at 60 °C. To obtain the $Pt_{SA/NP}$-$TiO_{2-x}B_x$ photocatalyst, the sample was annealed in air at 450 °C for 4 hours. The $Pt_{SA/NP}$-TiO_2 was synthesized using the same procedure as $Pt_{SA/NP}$-$TiO_{2-x}B_x$, with the only difference being the use of MIL-125(Ti_V) without B as the precursor for encapsulation.

Preparation of blank TiO_2 and $TiO_{2-x}B_x$

Blank TiO_2 and $TiO_{2-x}B_x$ were prepared by calcining the MIL-125 and B-MIL-125 at 450 °C for 4 hours, respectively.

Preparation of Pt_{SA}-$TiO_{2-x}B_x$

Typically, 4.5 mL of methanol, 40 mL of DMF, and 2.3 g of PTA were mixed under stirring. Subsequently, 0.96 mL of TBOT and a predetermined amount of H_2PtCl_6 (e.g., 3.7 mg for 0.2 wt.% Pt) were added to the solution. After stirring for 10 minutes, the mixture was transferred to a 100 mL Teflon-lined autoclave and heated at 130 °C for 20 hours. Upon completion of the hydrothermal reaction and natural cooling, the Pt_{SA}-MIL-125 was obtained. And B/Pt_{SA}-MIL-125 was then synthesized by introducing B via the same ligand exchange strategy. The resulting B/Pt_{SA}-MIL-125 was collected by centrifugation, washed with water, and dried at 60 °C. Finally, the sample was annealed in air at 450 °C for 4 hours to yield Pt_{SA}-$TiO_{2-x}B_x$.

Preparation of Pt_{NP}-$TiO_{2-x}B_x$

100 mg $TiO_{2-x}B_x$ were dispersed in 30 mL of DI water. A specific amount of H_2PtCl_6 (e.g., 2.64 mg for 1 wt.% Pt) was then added to the suspension. The container was then sealed, and the mixture was stirred under a 365 LED illumination for 12 h. After the reaction, the product was washed with water and then dried at 60 °C to obtain Pt_{NP}-$TiO_{2-x}B_x$.

Preparation of $Pt_{SA/NP}$@$TiO_{2-x}B_x$

To obtain the $Pt_{SA/NP}$@$TiO_{2-x}B_x$ photocatalyst (without B-Pt coordination), 50 mg of $TiO_{2-x}B_x$ was dispersed in 200 mL of DI water. A specific amount of H_2PtCl_6 (e.g., 1.32 mg for 0.6 wt.% Pt) was then added to the suspension, and the mixture was stirred in a dark environment for 1 hour, the resultant sample was washed with water and then dried at 60 °C to yield $Pt_{SA/NP}$@$TiO_{2-x}B_x$.

Characterizations

The structural, morphological, and surface properties of the catalysts were comprehensively characterized using a combination of techniques. Thermogravimetric analysis (TG-DTA, ZCT-B, Beijing) was employed to determine the thermal stability. X-ray diffraction (Rigaku, Cu Kα radiation) was employed to determine the crystallinity, and Raman spectra were collected with a LabRAM HR Evolution spectrometer (HORIBA, 532 nm laser). Morphology and microstructure were observed by scanning electron microscopy (SEM, Nova Nano SEM 450) and transmission electron microscopy (TEM, JEM-2100), with aberration-corrected HAADF-STEM imaging performed on a Titan Cubed Themis G2 300 (Thermo Fisher).

Optical absorption was analyzed by UV-vis diffuse reflectance spectroscopy (Metash UV-9000S, $BaSO_4$ as reference), and surface area and porosity were measured from N_2 adsorption-desorption isotherms at 77 K using a BET analyzer (3H-2000PS2). Surface chemical states were investigated by X-ray photoelectron spectroscopy (XPS, Thermo ESCALAB 250Xi, Al Kα), and elemental composition was determined by ICP-OES (Agilent 7700X). Magnetic properties were probed by a PPMS (DynaCool, Quantum Design), and paramagnetic centers were examined by electron paramagnetic resonance (EPR, Bruker EMXnano).

Synchrotron-based X-ray absorption spectroscopy was carried out to analyze Ti K-edge (RapidXAFS 2 M, Ge(311) analyzer) and Pt L_3-edge (BL11B beamline, SSRF, Si(311) monochromator) EXAFS and XANES spectra. In situ XPS was conducted under 300 W Xe lamp irradiation (Perfectlight PLS-SXE300C), and in situ EPR spectra were recorded in Ar-filled quartz tubes (Bruker ESR500, X-band).

The charge-carrier dynamics were further investigated by steady-state photoluminescence (PL, Shimadzu FL-4500, excitation 365 nm) and time-resolved PL (FLS 1000, Edinburgh Instruments, excitation 365 nm, emission 430 nm). The TRPL average lifetime (τ_{avg}) were fitted using equation:

$$I(t) = A_1 e^{-t/\tau_1} + A_2 e^{-t/\tau_2} \quad (1)$$

and the τ_{ave} is calculated by following equation:

$$\tau_{ave} = \frac{A_1\tau_1^2 + A_2\tau_2^2}{A_1\tau_1 + A_2\tau_2} \quad (2)$$

where A_1 and A_2 are the normalized amplitudes of the two decay components, and τ_1 and τ_2 are the corresponding lifetimes.

The characterization procedures were adapted from our previous reports[10,41].

Photocatalytic property evaluation

A multichannel photochemical system (PCX-50C, Discover, Perfect Light Ltd.) was used for conducting photocatalytic H_2 evolution (PHE) experiments. Typically, 5 mg of catalyst was dispersed in 30 mL of a water/methanol mixture (1:2, v/v) in a sealed quartz reaction vessel, followed by ultrasonic treatment for 3 min. The system was purged with Ar (10 cycles) to remove air before illumination. A 365 nm LED lamp (5 W) served as the light source, and the suspension was continuously stirred at 40 °C using a circulating water bath. The evolved H_2 was quantified every 10 min by gas chromatography (GC7900, TCD detector, Ar carrier gas). After each 1 h cycle, accumulated H_2 was purged with Ar, and the experiment was repeated three times to calculate the average H_2 evolution rate. For long-term stability tests, the catalyst loading was reduced to 2 mg to avoid excessive pressure from continuous H_2 generation.

The apparent quantum efficiency (AQE) was measured under monochromatic LED irradiation at 365, 385, and 420 nm with intensities of 62.4, 48.3, and 36.7 mW cm^{-2}, respectively. In a typical test, 10 mg of catalyst was used under the same conditions as the PHE experiment. The AQE was calculated using Eq. (3):

$$\mathrm{AQE} = \frac{2MN_A hc}{AIt\lambda} \times 100\% \quad (3)$$

where M is the amount of evolved H_2 (mol), N_A is Avogadro's constant, h is Planck's constant, c is the speed of light, I is the incident light intensity, A is the irradiation area, t is the reaction time, and λ is the irradiation wavelength. Each value was averaged from three independent measurements.

The turnover frequency (TOF) was determined using Eq. (4):

$$\mathrm{TOF} = \frac{n\mathrm{H_2}}{n\mathrm{Pt} \times t} \quad (4)$$

where $n$$H_2$ is the number of moles of H_2 generated, nPt is the number of moles of Pt in the catalyst, and t is the reaction time.

The photocatalytic testing protocols were adapted from our previous report[41] with minor modifications.

Photo-electrochemical measurements

Photoelectrodes were fabricated by dispersing 5 mg of catalyst in 5 wt.% Nafion ethanol solution and drop-casting the suspension onto fluorine-doped tin oxide (FTO) glass (2.0 × 2.5 cm^2), followed by drying at 60 °C for 3 h. Photoelectrochemical (PEC) tests were performed on a

CHI-760E electrochemical workstation in a standard three-electrode configuration, with the prepared electrode as the working electrode, Ag/AgCl (saturated KCl) as the reference electrode, and a Pt foil as the counter electrode.

The electrolyte was 0.20 M Na_2SO_4 (pH = 6.98 ± 0.13), prepared within 24 h prior to use by dissolving anhydrous Na_2SO_4 (5.68 g) in 200 mL of deionized water under magnetic stirring until fully dissolved. The solution was stored in a sealed amber polypropylene container at room temperature in the dark. The pH was measured at 25 °C with a three-point calibrated benchtop pH meter (buffers at pH 4.00, 7.00, and 10.00), and values are reported as mean ± SD from three independent measurements ($n = 3$).

Electrochemical impedance spectroscopy (EIS) was conducted with an AC perturbation of 5.0 mV in the frequency range of 10^5–0.1 Hz. Photocurrent responses under chopped illumination (150 W Xe lamp, 94.7 mW cm^{-2}) were recorded using the amperometric I-t method. Transient photocurrent measurements were collected at 1.0 kHz with an applied AC voltage of 5.0 mV.

The PEC measurement procedures were adapted from our previous work[41] with minor modifications.

CO adsorption infrared spectrum measurements

CO chemisorption measurements were conducted using diffuse reflectance infrared Fourier transform spectroscopy (DRIFTS) on a Bruker VERTEX 80 v spectrometer. To collect the CO-DRIFTS spectra, the sample was first reduced under a 10% H_2/Ar gas flow at 150 °C for 0.5 hour after being loaded into the reflectance cell. Following the pretreatment, the sample was cooled to 30 °C under an Ar atmosphere, and a background spectrum was recorded. The sample was then exposed to a 10% CO/Ar gas flow at 20 mL min^{-1} for approximately 1 h until adsorption saturation was reached. Subsequently, the sample was purged with Ar at a flow rate of 20 mL min^{-1} for an additional 40 min to remove gas-phase CO.

Isotopic experiment

The isotopic experiment was conducted using a multichannel photochemical reactor under 365 nm LED irradiation. Typically, 15 mg of sample was added to 30 ml reaction solution, followed by irradiation. Two parallel experiments were performed under identical photocatalytic conditions, replacing water and methanol with heavy water (D_2O) and deuterated methanol (CD_3OD) with same ratio, respectively. The evolved products were subsequently analyzed by mass spectrometry (MS, Hiden HPR-40).

Surface photovoltage (SPV) experiments

Samples were uniaxially pressed into dense pellets (diameter: 10 mm; thickness: 1 mm). Surface potentials (V_s) before and during illumination were performed using the SKP5050 Kelvin probe with a calibrated LED light source (wavelength: 365 nm). The measurement area of samples is a circular region with a diameter of 2 mm. The surface photovoltage (SPV) was calculated as:

$$SPV = V_s(\text{illumination}) - V_s(\text{darkness}) \quad (5)$$

where V(illumination) and V(darkness) are the measured surface potentials before and during illumination, respectively.

In-situ irradiated XPS measurements

In-situ irradiated XPS measurements were performed by a photoelectron spectrometer (ESCALAB 250Xi) with an Al Kα radiation source (hv = 1486.68 eV).

Survey spectra were acquired with a pass energy of 100 eV and a step size of 1 eV, while high-resolution spectra were collected at 20 eV with 0.05 eV steps. During the measurement, the non-irradiated XPS spectra were collected first, and then the irradiated XPS spectra were collected after irradiation for 30 minutes. The light source (300 W Xe-lamp) is installed on the outside of the XPS instrument, and the irradiated XPS data is collected while it is irradiated.

Computational methods and details

Density functional theory (DFT) calculations were performed with the Vienna Ab initio Simulation Package (VASP). The generalized gradient approximation (GGA) within the Perdew-Burke-Ernzerhof (PBE) scheme was adopted for exchange–correlation. A plane-wave basis set was used with an energy cutoff of 500 eV. Structural optimizations were converged to a precision of 1×10^{-5} eV and 0.02 eV·$Å^{-1}$. Electron states were sampled using a 1×2×1 k-point mesh centred at Γ. For Ti and Pt atoms, the U correction was applied with U values of 4.2 eV and 2.4 eV, respectively. A vacuum layer of 15 Å was employed in the surface model. After structure optimization, catalytic properties were evaluated by calculating the Gibbs free energy for H* adsorption.

$$\Delta G_{H^*} = \Delta E + \Delta ZPE - T\Delta S \quad (6)$$

where ΔE denotes the reaction energy difference, ΔZPE the zero-point energy correction, and ΔS the vibrational entropy contribution at temperature T. The atomic coordinates of all computational models are provided in Supplementary Data 1.

Data availability

The source data generated in this study are provided in the Source Data file. Source data are provided with this paper.

References

1. Zhou, P. et al. Solar-to-hydrogen efficiency of more than 9% in photocatalytic water splitting. *Nature* **613**, 66–70 (2023).
2. Li, Y. Y. et al. Electrolyte-assisted polarization leading to enhanced charge separation and solar-to-hydrogen conversion efficiency of seawater splitting. *Nat. Catal.* **7**, 77–88 (2024).
3. Lee, W. H. et al. Floatable photocatalytic hydrogel nanocomposites for large-scale solar hydrogen production. *Nat. Nanotechnol.* **18**, 754–762 (2023).
4. Wan, S. et al. A superlattice interface and S-scheme heterojunction for ultrafast charge separation and transfer in photocatalytic H_2 evolution. *Nat. Commun.* **15**, 9612 (2024).
5. Kosco, J. et al. Generation of long-lived charges in organic semiconductor heterojunction nanoparticles for efficient photocatalytic hydrogen evolution. *Nat. Energy* **7**, 340–351 (2022).
6. Sheng, H. X. et al. Strong synergy between gold nanoparticles and cobalt porphyrin induces highly efficient photocatalytic hydrogen evolution. *Nat. Commun.* **14**, 1528 (2023).
7. Ruan, X. W. et al. A Twin S-Scheme Artificial Photosynthetic System with Self-Assembled Heterojunctions Yields Superior Photocatalytic Hydrogen Evolution Rate. *Adv. Mater.* **35**, 2209141 (2023).
8. Song, S. et al. A selective Au-ZnO/TiO_2 hybrid photocatalyst for oxidative coupling of methane to ethane with dioxygen. *Nat. Catal.* **4**, 1032–1042 (2021).
9. Liu, B. X. et al. Regulating the Transfer of Photogenerated Carriers for Photocatalytic Hydrogen Evolution Coupled with Furfural Synthesis. *ACS Nano* **18**, 17939–17949 (2024).
10. Zhang, Y. M. et al. Single-atom Cu anchored catalysts for photocatalytic renewable H_2 production with a quantum efficiency of 56%. *Nat. Commun.* **13**, 58 (2022).
11. You, X. M. et al. Ultrahigh Bifunctional Photocatalytic CO_2 Reduction and H_2 Evolution by Synergistic Interaction of Heteroatomic Pt-Ru Dimerization Sites. *ACS Nano* **18**, 9403–9412 (2024).
12. Tang, M. H. et al. Upcycling of Polyamide Wastes to Tertiary Amines Using Mo Single Atoms and Rh Nanoparticles. *Angew. Chem. -Int. Ed.* **64**, e202416436 (2024).

13. Zhu, Y. H. et al. Synergistic Effect of Platinum Single Atoms and Nanoclusters Boosting Electrocatalytic Hydrogen Evolution. *CCS Chem.* **3**, 2539–2547 (2021).
14. Zhang, J. K. et al. Mechanistic Insight into the Synergy between Platinum Single Atom and Cluster Dual Active Sites Boosting Photocatalytic Hydrogen Evolution. *Adv. Mater.* **35**, 2300902 (2023).
15. Liu, P. G. et al. Synergy between Palladium Single Atoms and Nanoparticles via Hydrogen Spillover for Enhancing CO_2 Photoreduction to CH_4. *Adv. Mater.* **34**, 2200057 (2022).
16. Zhang, J. K., Zheng, X. H., Yu, W. L., Feng, X. & Qin, Y. Unravelling the synergy in platinum-nickel bimetal catalysts designed by atomic layer deposition for efficient hydrolytic dehydrogenation of ammonia borane. *Appl. Catal. B-Environ. Energy* **306**, 121116 (2022).
17. Xi, S. B., Zhang, J. & Xie, K. Low-temperature Water-gas Shift Reaction Enhanced by Oxygen Vacancies in Pt-loaded Porous Single-crystalline Oxide Monoliths. *Angew. Chem. -Int. Ed.* **61**, e202209851 (2022).
18. Lv, T. P. et al. Insights into synergistic effect of Pd single atoms and sub-nanoclusters on TiO_2 for enhanced photocatalytic H_2 evolution. *Chem. Eng. J.* **450**, 137873 (2022).
19. Yu, Y. Y. et al. Synergistic Effect of Cu Single Atoms and Au-Cu Alloy Nanoparticles on TiO_2 for Efficient CO_2 Photoreduction. *ACS Nano* **15**, 14453–14464 (2021).
20. Gao, Z. Y. et al. Photocatalytic Methanol Dehydrogenation Promoted Synergistically by Atomically Dispersed Pd and Clustered Pd. *J. Am. Chem. Soc.* **146**, 24440–24449 (2024).
21. Zhang, J. K. et al. Species Heterogeneity and Synergy to Boost Photocatalytic Hydrogen Evolution. *ACS Catal.* **14**, 15699–15712 (2024).
22. Ren, M. et al. Synergy between palladium single atoms and small nanoparticles co-anchored on carbon atom self-doped graphitic carbon nitride boosting photocatalytic H_2 generation. *Appl. Catal. B-Environ. Energy* **345**, 123680 (2024).
23. Wang, H. et al. High quantum efficiency of hydrogen production from methanol aqueous solution with PtCu-TiO_2 photocatalysts. *Nat. Mater.* **22**, 619–626 (2023).
24. Wang, W. Y. et al. Catalytic Refining Lignin-Derived Monomers: Seesaw Effect between Nanoparticle and Single-Atom Pt. *Angew. Chem. -Int. Ed.* **63**, e202404683 (2024).
25. Chen, C. L. et al. Asymmetrically Coordinated Cu Dual-Atom-Sites Enables Selective CO_2 Electroreduction to Ethanol. *Adv. Mater.* **36**, 2409797 (2024).
26. Niu, X. D., Wei, J., Xu, D. Y., Pei, J. J. & Sui, R. Charge-asymmetry Fe_1Cu single-atom alloy catalyst for efficient oxygen reduction reaction. *Nano Res* **17**, 4702–4710 (2024).
27. Zhang, W. J. et al. Regulating Hydrogen/Oxygen Species Adsorption via Built-in Electric Field-Driven Electron Transfer Behavior at the Heterointerface for Efficient Water Splitting. *Angew. Chem. -Int. Ed.* **63**, e202400888 (2024).
28. Zhai, H. H. et al. Electronic Regulation of Pt Single-Atom Catalysts via Local Coordination State Adjustment for Enhanced Photocatalytic Performance. *ACS Catal.* **13**, 8063–8072 (2023).
29. Wei, J. et al. Site-specific metal-support interaction to switch the activity of Ir single atoms for oxygen evolution reaction. *Nat. Commun.* **15**, 559 (2024).
30. Liu, W. J. et al. Regulating Local Electron Distribution of Cu Electrocatalyst via Boron Doping for Boosting Rapid Absorption and Conversion of Nitrate to Ammonia. *Adv. Funct. Mater.* **34**, 2408732 (2024).
31. Huang, L. et al. Precisely Regulating Asymmetric Charge Distribution by Single-Atom Central Doped Ag-Based Series Clusters for Enhanced Photoreduction of CO_2 to Alcohol Fuels. *Angew. Chem. -Int. Ed.* **63**, e202412964 (2024).
32. Song, G. X. et al. High-spin state Fe(III) doped TiO_2 for electrocatalytic nitrogen fixation induced by surface F modification. *Appl. Catal. B-Environ. Energy* **301**, 120809 (2022).
33. Gao, Y. X. et al. Regulating the electron spin orbital by sulfur doping of Ti vacancies to manipulate spin flip for enhancing PEC water splitting performance. *Energy Environ. Sci.* **17**, 6268–6278 (2024).
34. Zhang, R. X. et al. Direct Photocatalytic Methane Oxidation to Formaldehyde by N Doping Co-Decorated Mixed Crystal TiO_2. *ACS Nano* **18**, 12994–13005 (2024).
35. Zi, B. Y. et al. Pr doping promotes the formation of Pt single atoms by regulating metal-support interaction for remarkable photocatalytic hydrogen production. *J. Colloid Interface Sci.* **680**, 298–306 (2025).
36. Kerketta, U., Kim, H., Denisov, N. & Schmuki, P. Grätzel-Type TiO_2 Anatase Layers as Host for Pt Single Atoms: Highly Efficient and Stable Photocatalytic Hydrogen Production. *Adv. Energy Mater.* **14**, 2302998 (2024).
37. Liu, C. W. et al. Knowledge-Driven Design and Lab-Based Evaluation of B-doped TiO_2 Photocatalysts for Ammonia Synthesis. *Adv. Energy Mater.* **13**, 2204126 (2023).
38. Cheng, X. et al. Ligand Charge Donation-Acquisition Balance: A Unique Strategy to Boost Single Pt Atom Catalyst Mass Activity toward the Hydrogen Evolution Reaction. *ACS Catal.* **12**, 5970–5978 (2022).
39. Li, H., Qin, X. X., Zhang, X. G., Jiang, K. & Cai, W. B. Boron-Doped Platinum-Group Metals in Electrocatalysis: A Perspective. *ACS Catal.* **12**, 12750–12764 (2022).
40. Mao, Z. J. et al. Interstitial B-Doping in Pt Lattice to Upgrade Oxygen Electroreduction Performance. *ACS Catal.* **12**, 8848–8856 (2022).
41. Li, B. et al. Revealing the synergistic effect of bulk and surface co-doped boron on TiO_2 for enhanced photocatalytic H_2 evolution. *Chem. Eng. J.* **497**, 154726 (2024).
42. Li, Y. J. et al. Boron containing metal-organic framework for highly selective photocatalytic production of H_2O_2 by promoting two-electron O_2 reduction. *Mater. Horiz.* **8**, 2842–2850 (2021).
43. Ma, K. W. et al. Revealing different depth boron substitution on interfacial charge transfer in TiO_2 for enhanced visible-light H_2 production. *Appl. Catal. B-Environ.* **315**, 121570 (2022).
44. Guo, M. C. et al. Single-Atom Pt Loaded on MOF-Derived Porous TiO_2 with Maxim-Ized Pt Atom Utilization for Selective Hydrogenation of Halonitro-benzene. *Angew. Chem. -Int. Ed.* **64**, e202418964 (2025).
45. Jeong, H. et al. Controlling the Oxidation State of Pt Single Atoms for Maximizing Catalytic Activity. *Angew. Chem. -Int. Ed.* **59**, 20691–20696 (2020).
46. Si, Y. et al. Fully exposed Pt clusters for efficient catalysis of multi-step hydrogenation reactions. *Nat. Commun.* **15**, 4887 (2024).
47. Kim, T. S., O'Connor, C. R. & Reece, C. Interrogating site dependent kinetics over SiO_2-supported Pt nanoparticles. *Nat. Commun.* **15**, 2074 (2024).
48. Macino, M. et al. Tuning of catalytic sites in Pt/TiO_2 catalysts for the chemoselective hydrogenation of 3-nitrostyrene. *Nat. Catal.* **2**, 873–881 (2019).
49. Chen, J. J. et al. Reverse oxygen spillover triggered by CO adsorption on Sn-doped Pt/TiO_2 for low-temperature CO oxidation. *Nat. Commun.* **14**, 3477 (2023).
50. Zhang, J. J., Zhang, L. Y., Wang, W. & Yu, J. G. In Situ Irradiated X-ray Photoelectron Spectroscopy Investigation on Electron Transfer Mechanism in S-Scheme Photocatalyst. *J. Phys. Chem. Lett.* **13**, 8462–8469 (2022).
51. Zhang, J. Y. et al. Electronic and transport properties of Li-doped NiO epitaxial thin films. *J. Mater. Chem. C.* **6**, 2275–2282 (2018).
52. Zhang, Z. & Yates, J. T. Band Bending in Semiconductors: Chemical and Physical Consequences at Surfaces and Interfaces. *Chem. Rev.* **112**, 5520–5551 (2012).

53. Liu, D. J. et al. Modulating local coordination structure over single Pt atom to optimize adsorption behavior for high-efficiency photocatalytic H_2 production. *Appl. Catal. B-Environ. Energy* **361**, 124655 (2025).
54. Da, Y. M. et al. Single-Atom Pt Doping Induced p-Type to n-Type Transition in NiO Nanosheets toward Self-Gating Modulated Electrocatalytic Hydrogen Evolution Reaction. *ACS Nano* **17**, 18539–18547 (2023).
55. Zhao, Y. L. et al. Vacancy Defects Inductive Effect of Asymmetrically Coordinated Single-Atom Fe-N_3S_1 Active Sites for Robust Electrocatalytic Oxygen Reduction with High Turnover Frequency and Mass Activity. *Adv. Mater.* **36**, 2308243 (2024).
56. Pan, L. et al. Manipulating spin polarization of titanium dioxide for efficient photocatalysis. *Nat. Commun.* **11**, 418 (2020).
57. Wu, H. et al. Strong intrinsic room-temperature ferromagnetism in freestanding non-van der Waals ultrathin 2D crystals. *Nat. Commun.* **12**, 5688 (2021).
58. Sun, T. et al. Ferromagnetic single-atom spin catalyst for boosting water splitting. *Nat. Nanotechnol.* **18**, 763–771 (2023).
59. Sun, K. et al. Manipulating the Spin State of Co Sites in Metal-Organic Frameworks for Boosting CO_2 Photoreduction. *J. Am. Chem. Soc.* **146**, 3241–3249 (2024).
60. Chen, F., Ma, T. Y., Zhang, T. R., Zhang, Y. H. & Huang, H. W. Atomic-Level Charge Separation Strategies in Semiconductor-Based Photocatalysts. *Adv. Mater.* **33**, 2005256 (2021).
61. Jiang, X. H. et al. Silver Single Atom in Carbon Nitride Catalyst for Highly Efficient Photocatalytic Hydrogen Evolution. *Angew. Chem. -Int. Ed.* **59**, 23112–23116 (2020).
62. Luo, H. et al. Pt single-atoms supported on nitrogen-doped carbon dots for highly efficient photocatalytic hydrogen generation. *J. Mater. Chem. A* **8**, 14690–14696 (2020).
63. Chen, R. T. et al. Spatiotemporal imaging of charge transfer in photocatalyst particles. *Nature* **610**, 296–301 (2022).
64. Chen, R. T., Fan, F. T., Dittrich, T. & Li, C. Imaging photogenerated charge carriers on surfaces and interfaces of photocatalysts with surface photovoltage microscopy. *Chem. Soc. Rev.* **47**, 8238–8262 (2018).
65. Tousek, J. & Tousková, J. A novel approach to the surface photovoltage method. *Sol. Energy Mater. Sol. Cells* **92**, 1020–1024 (2008).
66. Zhang, L. Y., Zhang, J. J., Yu, J. G. & Garcia, H. Charge-transfer dynamics in S-scheme photocatalyst. *Nat. Rev. Chem.* **9**, 328–342 (2025).
67. Kumar, C. P., Gopal, N. O., Wang, T. C., Wong, M. S. & Ke, S. C. EPR investigation of TiO_2 nanoparticles with temperature-dependent properties. *J. Phys. Chem. B* **110**, 5223–5229 (2006).
68. Berger, T. et al. Light-induced charge separation in anatase TiO_2 particles. *J. Phys. Chem. B* **109**, 6061–6068 (2005).
69. Li, J. J. et al. Highly Active and Stable Metal Single-Atom Catalysts Achieved by Strong Electronic Metal-Support Interactions. *J. Am. Chem. Soc.* **141**, 14515–14519 (2019).
70. Long, H. Y. et al. Fine-tuning *d-p* hybridization in Ni-B_x cocatalyst for enhanced photocatalytic H_2 production. *Nat. Commun.* **16**, 946 (2025).
71. Li, M. Y. et al. Engineering Spatially Adjacent Redox Sites with Synergistic Spin Polarization Effect to Boost Photocatalytic CO_2 Methanation. *J. Am. Chem. Soc.* **146**, 15538–15548 (2024).

Acknowledgements

This work was supported by the National Key Research and Development Program of China (2022YFB3803600 (Q.L.[1,2*])), the National Natural Science Foundation of China (22378346, 22368050 (Q.L.[1,2*])), the Key Research and Development Program of Yunnan Province (202302AF080002 (Q.L.[1,2*])), and Scientific Research and Innovation Project of Postgraduate Students in the Academic Degree of Yunnan University (KC-24248466 (B.L.)). Authors thank the Electron Microscopy Center, the Advanced Computing Center, the Advanced Analysis and Measurement Center of Yunnan University for the sample testing and computations service.

Author contributions

B.L., T.Z., and Q.L.[1,2*] conceived and designed the study. H.Z. and T.H. carried out the synthesis theory calculations of the study. Q.L.[1], D.L., and B.Z. carried out the synthesis and characterizations of the materials. B.L., and M.Z. carried out the photocatalytic test. M.C, Y.Z[1]., H.S, Y.Z[3], J.Z., Z.Z., G.Z., and J.H.Z. contributed to data analysis. T.Z. and Q.L.[1,2*] supervised the project. B.L. wrote the manuscript. B.L., T.Z., and Q.L.[1,2*] revised and reviewed the manuscript. All authors discussed the results and commented on the manuscript.

Competing interests

The authors declare no competing interests.

Additional information

Supplementary information The online version contains supplementary material available at https://doi.org/10.1038/s41467-025-63637-2.

Correspondence and requests for materials should be addressed to Tong Zhou or Qingju Liu.

Peer review information *Nature Communications* thanks Kenichi Ozawa and the other anonymous reviewer(s) for their contribution to the peer review of this work. A peer review file is available.